Pedro Alexandre Aparício de Moura

Bachelor in micro and nanotechnology engineering

Simulation and optical characterization of efficient light-emitting metallo-dielectric micro- and nanopillars

Dissertation to obtain a master's degree in
Micro and nanotechnology engineering

Supervisor: Dr. Jana B. Nieder, Research Group Leader, INL - International Iberian Nanotechnology Laboratory

Co-supervisor: Dr. Bruno Romeira, Staff Researcher, INL - International Iberian Nanotechnology Laboratory

Dr. Manuel Mendes, Assistant professor, FCT-NOVA

Presidente: Dr. Luís Miguel Nunes Pereira

Arguentes: Dr.José Figueiredo

Vogais: Dr.Bruno Romeira

Setembro, 2019

FACULDADE DE CIÊNCIAS E TECNOLOGIA
UNIVERSIDADE NOVA DE LISBOA

Simulation and optical characterization of efficient light-emitting metallo-dielectric micro- and nanopillars

“A lesson without pain is meaningless. That's because no one can gain without sacrificing something. But by enduring that pain and overcoming it, he shall obtain a powerful, unmatched heart. A fullmetal heart.”

- Hiromu Arakawa

Acknowledgements

In September 2014, a new stage began in my life that brought me besides the knowledge and responsibility, great friends that I will take for my life.

First of all, I want to thank my academic supervisor Dr. Manuel Mendes and my supervisors at the INL - International Iberian Nanotechnology Laboratory, where this research project was conducted, Dr. Jana B. Nieder and Dr. Bruno Romeira, that they offered me the opportunity to work on an exciting research topic and gave access to all the required knowledge and research facilities.

Importantly I want to thank the university where I studied, UNL – FCT (Faculty of Science and Technology) for all the opportunities. To every professor, along the past 5 years, I am deeply grateful for the knowledge that was passed on to me and will certainly help me in the future. I want also to thank the many friends for the companionship and friendship some of them for more than just this 5 year, Sofia, Tiago, Leonor, André, Carlos, Jorge, Pedro.

Secondly, I want to thank the INL, specially the Ultrafast Bio- and Nanophotonics group (Ricardo, Óscar, Sasha, Ânia, Manuel, Christian, Filipe, Rajesh, Carlota, Ima), for giving me the opportunity to learn and grow as person during almost 8 months. I want to give a special thanks to my supervisors Dr. Jana B. Nieder and Dr. Bruno Romeira, who were always available to support me in my work. I could not do it without them. I am deeply grateful for the opportunities of contributing to this great research group.

I thank INL and the Ultrafast Bio- and Nanophotonic group for providing access and training at the state-of-the-art nanofabrication and nanocharacterization facilities namely to the INL corporate labs "Clean room" and "Nanophotonics and Bioimaging".

Still from INL I want to thank some of my student's friends such as Rodrigo, Sara, João, António, Fay, Beatriz and Anastasia.

Last but most important I want to thank my family. My dad, my mother and my sister, the 3 most important persons in my life, helped me unconditionally, giving me everything that I needed to be successful. I am deeply grateful for always being there supporting me and helping me in the good and bad moments.

Abstract

Currently there is a large boost in developing photonic technologies for computing as they promise high speed and low energy consumption. Nanoscale light sources might play a key role for such photonic integrated circuits, which may replace electronic chips one day. Recent experimental implementations include nanolasers, which typically require complex nanostructures for lasing operation, e.g. realized via photonic crystals, metallo-dielectric or plasmonic cavities.

Here alternatives to nanolasers are studied - nanolight-emitting diodes (nanoLEDs). The main advantages are that these do not require high quality factor cavities needed to reach a lasing threshold, thus making nanoLEDs less sensitive to fabrication imperfections. By engineering nanoLEDs using nanocavities, the spontaneous emission rate can be increased substantially as compared with the bulk material as described by the Purcell effect. NanoLEDs using cavities smaller than the emitted wavelength, show great potential due to their unique features such as ultra-small footprint, high-speed modulation and unprecedent low energies budget.

In this thesis, the optical properties of a dielectric encapsulated semiconductor AlGaAs/GaAs/AlGaAs nanopillars with or without a metal cavity will be investigated, both theoretically and experimentally. The theoretical part includes the analysis of metallo-dielectric micro- and nanopillar structures using 3D-FDTD simulations and the study of the radiative recombination taking the Purcell effect into account. The optical characterization includes the study of the emission properties using micro-photoluminescence and time-resolved photoluminescence techniques. From these results, the expected internal quantum efficiency (IQE) values are analyzed and the potential of these structures for the design of efficient nanoLED sources is discussed.

The results are discussed in the perspective of the development of highly efficient nanoLEDs at room-temperature for future integrated photonics circuits.

Keywords: (Photonics, NanoLED, Purcell effect, metallo-dielectric cavities, Internal Quantum Efficiency)

Resumo

Atualmente, temos assistido a um desenvolvimento crescente das tecnologias fotónicas para fins computacionais, uma vez que estas possibilitam larguras de banda muito elevadas e um consumo energético reduzido. Desta forma, as fontes de luz à nano-escala poderão desempenhar um papel fundamental em circuitos fotónicos integrados, podendo mesmo vir a substituir os chips eletrónicos em muitas das aplicações. As demonstrações experimentais mais recentes usam nanolasers, que normalmente requerem nano-estruturas complexas para obter emissão estimulada, que incluem cavidades utilizando cristais fotónicos, cavidades metalo-dielétricas ou plasmónicas.

No presente trabalho são estudados díodos emissores de luz à nano-scala, os nanoLEDs, enquanto alternativa aos nanolasers. Ao contrário dos nanolasers, os nanoLEDs não necessitam de cavidades com fatores de qualidade (Q) elevados, essenciais para se atingir o limiar de operação *laser*, tornando-os, por isso, menos sensíveis às imperfeições de fabrico. Para além disto, ao projetar nanoLEDs usando nanocavidades, a taxa de emissão espontânea pode ser aumentada em comparação com o material no *bulk*, como é descrito pelo efeito de Purcell. Assim, nanoLEDs constituídos por cavidades, cujas dimensões são menores que o comprimento de onda de luz emitido, mostram um grande potencial, tendo em conta características únicas como velocidade de modulação elevada, tamanhos reduzidos e consumos energéticos muito baixos.

Neste sentido, neste trabalho são investigadas, a nível teórico e experimental, as propriedades óticas de um nanopilar semicondutor AlGaAs/GaAs/AlGaAs encapsulado com um material dielétrico, utilizando ou não uma cavidade metálica. A parte teórica inclui a análise de micro e nanopilares envoltos por uma cavidade metalo-dielétrica através de simulações 3D-FDTD de forma a estudar o comportamento radiativo, tendo em conta o efeito de Purcell. A parte experimental abrange o estudo das propriedades óticas, usando técnicas de micro-fotoluminescência e fotoluminescência variável no tempo, de forma a estudar o comportamento não radiativo, nomeadamente, a recombinação não radiativa próxima da superfície das paredes dos pilares. A partir destes resultados, os valores esperados de eficiência quântica interna (EQI) serão analisados.

Finalmente, os resultados serão discutidos com vista ao desenvolvimento de nanoLEDs eficientes à temperatura ambiente para futuros circuitos fotónicos integrados.

Palavras-chave: (Fotónica, NanoLED, Efeito de Purcell, Cavidade metalo-dieléctrica, Eficiência quântica interna)

Table of Contents

Tables

Figures

1. Introduction

1.1 Light and photonic integration

The Moores's Law, an observation made by Gordon Moore in 1965, describes that the density of transistors, clock speed and power efficiency of an integrated circuit (IC) would double each 2 years, later changed to each 18 months [1],[2],[3].

Nowadays, we are witnessing a slowing down in the shrinking of complementary metal-oxide-semiconductor (CMOS) devices which may result in the end of Moore's law. In "Why is CMOS scaling coming to an end" [3], the challenges that CMOS technology is facing are explained including at least 3 major reasons: i) fundamental quantum limits beyond which transistors cannot be miniaturized, ii) device packing density limits due to local energy dissipation, and iii) the large overall energy consumption is becoming prohibitive due to the dense wired interconnects.

Photonic integrated circuits (PICs) combined with ICs appear as a promising solution to the limitations of ICs. The use of photons, which have a non-interacting bosonic nature, is advantageous as a signaling mechanism to overcome fan-out and parasitic constrains of electrical signals [4]. Current photonic technologies, which are optimized for long distance telecommunication and data communication applications, do not meet the necessary metrics (footprint, power dissipation, cost, and signal integrity) needed for interconnects between high-speed electronic chips. Ideally, future generations of computing systems will rely on optical interconnects [5],[6].

Figure 1 shows a schematic of a complete chip-to-chip interconnect link consisting of a modulated optical source, passive components to route the light, a photodiode for detection, and electronics for the driving circuitry. Despite many efforts, efficient optical interconnect links will require at least a 100-fold reduction of size as compared to existing photonic components (e.g. lasers, LEDs, photodetectors) in order to consume much less energy, and therefore lowering substantially the power consumption [5]. The only solution to solve this bottleneck is to develop radically new efficient and fast miniaturized (sub-μm^2) light sources and detectors, which will enable much lower energy to transfer data over short ranges of multi-processor systems [7]. Therefore, in future PIC platforms one would like to develop light sources that are efficient (10 fJ/bit) at low powers (~µW) and nanoscale in size for high integration density.

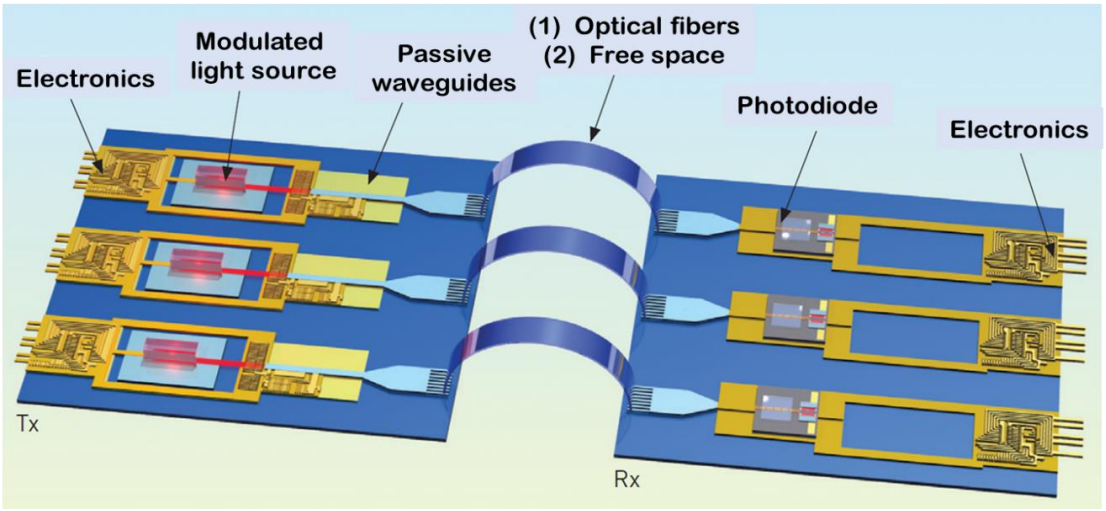

Figure 1 – Schematic of a chip-to-chip optically interconnected link (adapted from [7]).

1.2 Motivation and brief overview of nanoscale light sources

In laser technology there is clearly a drive for small coherent laser sources for many low power applications. A smaller laser requires less power and can potentially be switched on and off faster. The future on-chip or off-chip optical interconnects require light sources with areas below 10 μm², working efficiently at low output powers (in the order of 10-100 fJ/bit), and with densely spaced photonic wires to allow intermediate wire interconnects at 100 Gb/s/μm [5]. The first laser with a wavelength-scale optical mode was the vertical cavity surface emitting laser (VCSEL) [8]. Scaling light sources to the sub-micrometer range, and therefore shrinking an optical mode below the diffraction limit ~(λ/2n)3, where λ is the wavelength and n the refractive index in the material, requires more advanced optical confinement methods, such as 2-D or 3-D photonic crystals (PhCs), Figure 2(a), the use of metallo-dielectric cavities, Figure 2(b), or plasmonic resonances, Figure 2(c), and indeed, such methods have been employed to fabricate nanoscale lasers (see [9] for a recent review).

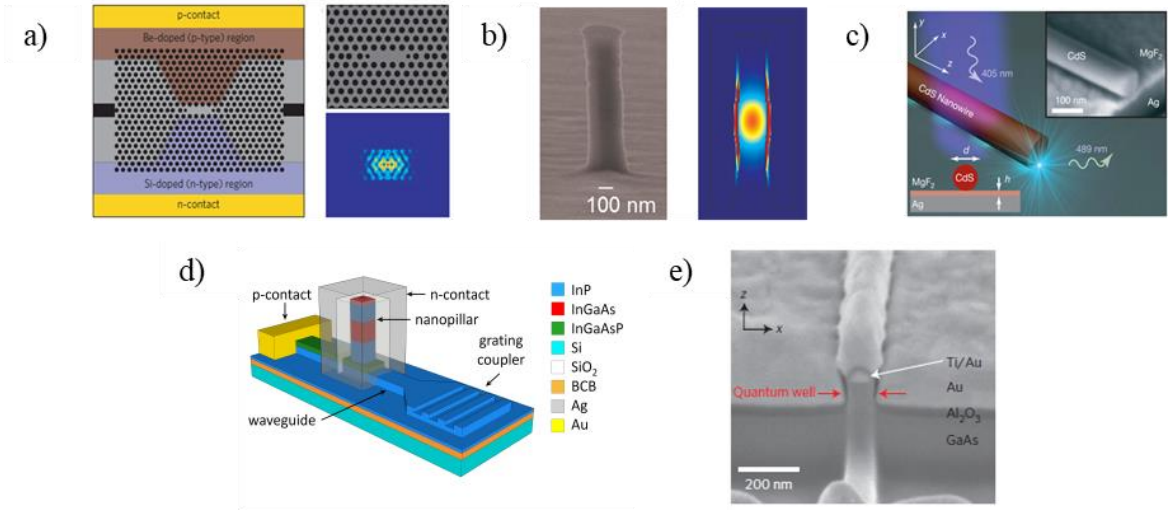

Figure 2 – Examples of a few representative structures of nanolasers using a) photonic crystals [10], b) metallo–dielectric [11], and c) plasmonic nanocavities [12]. It is also shown a few representative of nano-LEDs using d) metallo-dielectric [13] and e) plasmonic cavities [14].

Despite many progresses, as theoretical demonstrated in [15], aggressive scaling of lasers well below the wavelength (therefore in the plasmonic regime) will result in unacceptably high threshold current densities. In this context, it has been suggested the use of nanoscale light-emitting diodes, nanoLEDs Figure 2 (d) and (e), instead of nanolasers for on-chip communication systems requiring much low power consumption [15][16] .

1.3 Nanoscale light-emitting diodes (nanoLEDs)

An LED uses spontaneous emission, **Figure 3**(a), instead of stimulated emission, **Figure 3**(b). Therefore, unlike lasers, LEDs do not exhibit a threshold and can therefore be efficient at low current injection levels, do not require low-loss cavities and are therefore less sensitive to fabrication imperfections. Also, their broadband emission is not as much a concern for on-chip short distances where the effect of dispersion is minimal. Nevertheless, they have not been used for conventional high-speed communications because spontaneous emission is generally slower than stimulated emission. However, as analyzed in this thesis, the rate of spontaneous emission depends not only on the emitter itself but also on its optical environment. By properly engineering the optical density of states using a small cavity, **Figure 3**(c), the spontaneous emission rate of nanoscale LEDs can be increased substantially, making it competitive with stimulated emission.

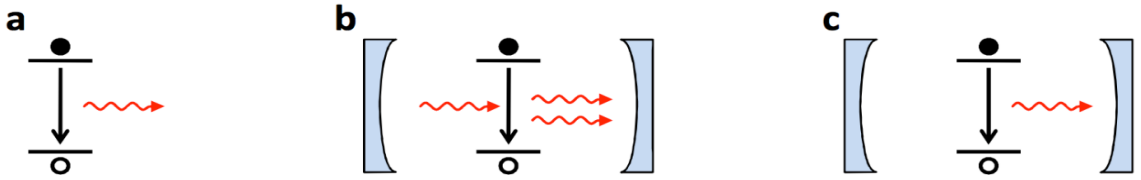

Figure 3 - Schematic of optical emitters: a) Spontaneous emission, b) Stimulated emission, c) Cavity-enhanced spontaneous emission. Reproduced from [16].

Neglecting aspects related to carrier injection efficiency and outcoupling efficiency in nanoLEDs, the efficiency of a nanoLED depends on its internal efficiency (IQE), and is given by:

$$IQE = \frac{\tau_r^{-1}}{\tau_r^{-1} + \tau_{nr}^{-1}} \quad (1)$$

where τ_r is the radiative lifetime and τ_{nr} is the nonradiative carrier lifetime. An added benefit of the size reduction is that the rate of spontaneous emission scales inversely with the mode volume, leading to faster and more efficient light emitters. In the case of LEDs, the increase in the spontaneous emission rate, τ_r, (also known as "Purcell effect") has been suggested as a method to make emission into a given mode the dominant recombination process, and thereby improve the efficiency of nanoLEDs to the levels typical of lasers [16] . This effect was first noted by Purcell which identified that by placing the emitter in cavity, the photonic density of states can be enhanced by a factor ∝Q/V over free space, the famous "Purcell factor".

Going from micro- to nanoscale LEDs, the surface-to-volume ratio increases substantially, as a result, surface properties become more relevant than volume properties meaning that, large surface recombination rates will have a decisive role on the efficiency of nanoLEDs. Surface recombination is promoted due to dangling bonds that often appear at the surface of structures, particularly for the case of the semiconductor material studied in this thesis. This increase is one of the challenges of scaling down LED´s sources [17]. One approach to reduce this problem is the use of a core/shell structure to avoid having the carriers away from the surface [18], or other chemical surface passivation methods [17].

Considering the aforementioned challenges in the design of efficient nanoLEDs, specifically i) increase the spontaneous emission in nanocavities, and ii) reducing the nonradiative effects, in this thesis a comprehensive studied on the optical properties in micro- and nanopillar semi-conductor structures was realized when a metal-cavity surrounds an AlGaAs/GaAs/AlGaAs semiconductor material. The studied devices are based on a novel design of a metallo-dielectric nanopillar cavity nanoLED using a combination of dielectric and metallic layers strong confinement of the optical mode in an ultrasmall volume (typically the nanopillar has a diameter of 300 nm). The design studied here is similar to the first metal-cavity laser reported by M.Hill et al in 2017 [11] and the first waveguide-coupled nanopillar metal-cavity nanoLED in 2017 [13]. However, these previous studies where targeting light sources operating at ~1550 nm and using InP-based materials. This work targets nanoLEDs operating at ~850 nm for short distance optical interconnects using GaAs-based materials.

The studies presented in this thesis can have an impact in the development of novel optical sources for optical interconnects, biophotonics and neuromorphic computing applications. The work of this thesis was realized in the framework of the European Union project ChipAI that targets to develop new photonic components, namely to use nanoLEDs emulating the behavior of neurons as the hardware for artificial intelligence (AI) systems [19]. The insights provided by the studies presented in this thesis, specifically the optical properties of metallo-dielectric nanopillar LED structures, will be applied onto the future development of these novel energy-efficient and high-bandwidth neuromorphic nanoLED devices.

1.4 Thesis outline

In this master thesis, the optical properties of metallic-cavity semiconductor nanopillars will be investigated, both theoretically and experimentally, towards the development of highly efficient nanoLEDs at room temperature. The thesis is divided as follows:

Chapter 2: Section 2.1 provides a brief overview of the radiative and nonradiative recombination processes occurring in wavelength-scale and sub-wavelength scale cavities. Section 2.2 describes the design of a metallo-dielectric nanopillar LED structure using III-V GaAs/AlGaAs compound semiconductor materials. Section 2.3 describes the 3-dimensional finite-difference time domain (FDTD) to simulate the optical field distribution of metallo-dielectric nanopillar structures. Lastly, section 2.4 provides the description of the - optical characterization methods of the fabricated micro- and nanopillar semiconductor structures.

Chapter 3: Reports and discusses: i) optical simulations of metallo-dielectric micro- and nanopillar structure using 3D FDTD simulations namely the results of the optical field distribution, the Q-factor, resonance frequency, Purcell effect and mode volume to study the radiative recombination behaviour; ii) optical characterization of micro- and nanopillar semiconductors using micro-photoluminescence and time-resolved photoluminescence experiments where the emission properties such as lifetimes and peak intensity in order to study nonradiative recombination behavior. Lastly, from the experimental and theoretical results achieved, the expected internal quantum efficiency (IQE) values are analyzed and the potential of these structures for the design of efficient nanoLED sources is discussed.

Chapter 4: Summarizes the results and conclusions reported in the thesis and future perspectives.

2. Material and Methods

2.1 Theory

Semiconductor nano-LEDs, with dimensions smaller than the emitted wavelength, show great potential due to their unique features including ultra-small footprint, high-speed modulation and unprecedented low energy budgets [17]. They appeared recently as light source alternatives to the high power consumption nanolasers since nano LEDs do not have threshold like lasers do [6].

The carrier recombination process rate in the active region of a semiconductor material depends on several mechanisms including spontaneous recombination rate, R_r, and, the nonradiative recombination, R_{nr}. The rate equation for carrier density, N, is given by [20]:

$$\frac{dN}{dt} = -(R_{nr} + R_r) = -\left(\frac{A}{V_a}v_s N + CN^3 + R_r\right) \quad (2)$$

where N is the carrier concentration in cm^3, A is the surface area of the active region, V_a is the volume of the active region, v_s is the surface velocity and C is the Auger emission coefficient [20][21]. R_r is the radiative recombination and is given by $\sim BN^2$, where B stands for bimolecular recombination coefficient and the typical values for III-V semiconductors are in the range between $10^{-11} - 10^{-9} cm^3/s$ [22]. In this thesis we test low carrier density (i.e. a nanoLED under low pumping conditions) and therefore will neglect Auger recombination effects since it is only relevant for the case of relatively high carrier concentration. In what follows we describe in more detail the process of surface recombination and radiative emission in nano-LED devices.

2.1.1 Nonradiative recombination in nano-LEDs

The interface between the semiconductor and the outside world is an inherent source of deep-level defects, commonly called surface states. These states are caused by dangling bonds at the crystal surface that result from the interruption of periodicity. Besides the inherent defects from the break in periodicity in semiconductors, other effects as a result of processing of semiconductors, specifically reactive ion plasma etching processes during fabrication can contribute to increase these defects. For calculation of the surface recombination, we define a capture rate of carriers located within some capture length of the surface. A larger capture length allows surface states to capture more carriers per unit time and hence leads to a higher capture rate. Because of the units, this capture rate is referred to as a velocity. The surface recombination in the situation where the exposed surface area is a pillar-type nano-LED geometry, as the one analyzed in this thesis, is given by:

$$R_{sr} = \frac{A}{V_a}v_s N = \frac{4}{d}v_s N \quad (3)$$

Where d is the pillar width. Clearly, for small scale nano-LEDs, as the surface-to-volume ratio increases substantially (corresponding to a very small d), the surface recombination plays a key role in the optical properties of the LEDs.

2.1.2 Radiative recombination in nano-LEDs

When it comes to the radiative recombination, in this thesis we investigate how the spontaneous emission of nano-LEDs is affected by the presence of a cavity, in this case a metallo-dielectric cavity. On the other hand, we want to understand the effect of the surface recombination in the efficiency of nanopillar LEDs. As discussed in the Introduction section, for a system coupled to an electromagnetic resonator the spontaneous emission probability can be increased over its bulk value. This is known as the Purcell factor [23] and can generally defined as [24]:

$$F = \frac{R_{sp,cav}}{R_{Bulk}} \quad (4)$$

The Purcell factor is calculated as the ratio of the spontaneous emission in a cavity over the spontaneous emission of the same bulk material. In the recent field of nanoscale light sources, the Purcell effect has been exploited to reduce the lasing threshold values of nanolasers [10], and increase the modulation speeds of nanolasers and nanoLEDs [25] and [26]. The rate of spontaneous emission in the bulk material can be approximated as BN^2 . The rate of spontaneous emission of an atom in a resonant cavity is directly calculated from the Fermi's Golden rule [24]:

$$R_{sp,cav} = \frac{2\pi}{\hbar^2}\int_0^{\infty} |< f|H|i >|^2 \rho(\omega)\, L(\omega) d\omega \tag{5}$$

where ρ(ω) is the density of optical states per unit of angular frequency, ω, $L(\omega)$ is the homogeneous broadening line shape, H is the atom-field interaction Hamiltonian and f and i are the final and initial states of the transition. In the most realistic case of nano-LEDs operating at room-temperature, the emitter width is broader than the single cavity mode width, **Figure 4**. This occurs for the typical cases of thermally broadened bulk or quantum well active layers [24].

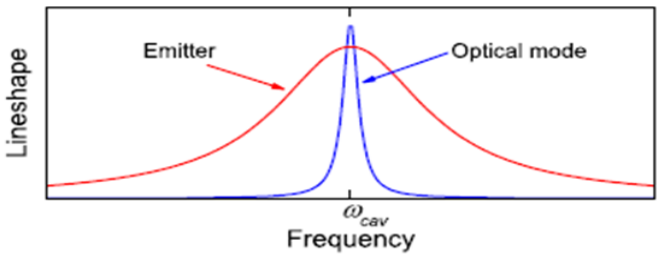

Figure 4 - Relation between the cavity resonance and the emitter's transition spectrum where the emitter's width is broader than the single cavity mode width (adopted from [24])

In our case, we are in a situation of a broad emitter in a narrow cavity. Assuming that $L(\omega)$ follows a Lorentzian centered at $\omega = \omega_{cav}$, where ω_{cav} is the cavity frequency, and ρ(ω) is approximated by a Dirac delta function centered at $\omega = \omega_{cav}$, the spontaneous emission in a cavity can be now derived using equation (5), which gives[24]:

$$R_{sp,cav} = \frac{2}{\hbar\varepsilon_o\varepsilon_r} d_{if}^2 \frac{\omega_{cav}}{\Delta\omega_{em}} \frac{1}{V} \tag{6}$$

Where $\hbar$ stand for the reduced Planck's constant, ε_o and $\varepsilon_r$are the permittivity in free space and in the active material, respectively, and d_{if} is the atomic dipole momentum. The parameter ω_{cav} stands for resonance frequency of the cavity, $\Delta\omega_{em}$ is the emitter linewidth, and finally V stands for the volume of the mode for that frequency. Physically, the cavity mode is a spatial distribution of electromagnetic energy. Its calculation, particularly in three-dimensional (3D) cavities generally requires use of numerical methods due to the geometric and material complexity of the cavities. When analyzing large cavities, the mode, is said to be approximately the physical size of the volume of the structure. However, for nano-cavities the mode volume can be much smaller than the physical cavity. The mode volume is calculated as:

$$V = \frac{\int \varepsilon(\boldsymbol{r})|\boldsymbol{E}(\boldsymbol{r})|^2 d^3\boldsymbol{r}}{max\,(\varepsilon|\boldsymbol{E}(\boldsymbol{r})|^2)} \tag{7}$$

Where $\boldsymbol{E}$ is the electric field and $\boldsymbol{r}$ is the position vector. This expression defines the mode volume as the ratio of total electrical energy to the peak value of electrical energy density. This expression will be applied to the metallic-dielectric structures for the case where the peak electric field resides in the active region of the semiconductor since, electric fields outside the active region quickly converge to zero, that is, only photonic modes are present in these structures. For the plasmonic case (not analyzed here and where the peak of the field resides between the dielectric and the metal) absorption from the metal also needs to be considered in the calculation of Eq. (6).

Equation (6) shows that the spontaneous emission processes depend inversely on the emitter's linewidth $\Delta\omega_{em,}$ depend directly on the resonant frequency ω_{cav} and depend inversely in V but not on the cavity Q-factor. This dependence $\propto \frac{1}{V}$ contrasts with the usual dependence of $\propto \frac{Q}{V}$, associated with the Purcell factor [23]. The usual dependence is valid assuming a Lorentzian DOS distribution with quality factor Q and an atom at resonance spectrally narrower than the cavity and spatially aligned with one anti-node of a cavity field. In the case of an emitter broader than the cavity, as the case analyzed in this thesis, there is not a sufficient interaction between the emitter and cavity and so the quality factor can be neglected in the calculation of the rate of spontaneous emission in a cavity.

2.2 Simulation of metallo-dielectric cavity nanoLED

In this work a study of the emission properties of a metallo-dielectric LED nanocavity was realized. This cavity device has a pillar-type geometry that consists of a III-V semiconductor, gallium arsenide (GaAs) and aluminum gallium arsenide (AlGaAs), forming an heterostructure, capped with a dielectric layer (typically SiO_x or SiN_x) followed by metal coating (e.g. Au or Ag). The presence of the metal enables to confine the light in structures with sub-µm dimensions, i.e., smaller that the wavelength. For this study, since the size of the structure was comparable to the wavelength, 3D finite difference time domain (FDTD) analysis from Lumerical [27] software was used (described in the next sub-section) to simulate the optical field distribution of these structures.

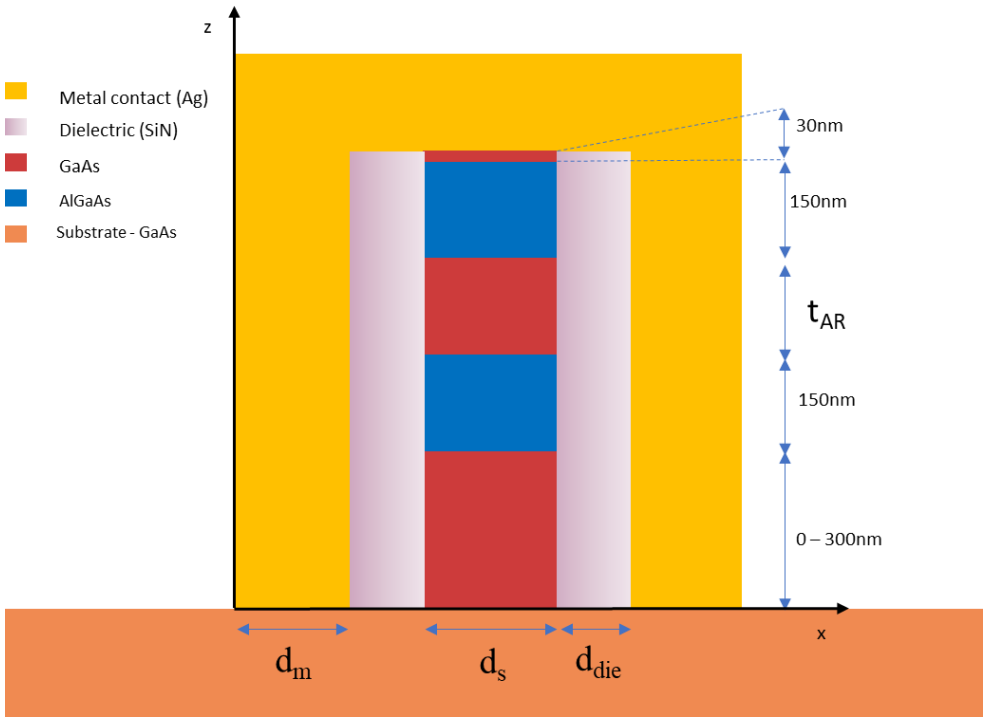

Figure 5 - Schematic of a metallo-dielectric light-emitting diode nanocavity structure.

Figure 5 presents the studied metallo-dielectric structure forming the nanolight-emitting diode showing the respective dimensions and materials. The targeted emission from these devices was around 850 nm, emitting from the middle GaAs emitting layer. The metal-dielectric semiconductor cavity structure consists of three main regions:

1) **Semiconductor region**: the central semiconductor region consists of (bottom to top) a GaAs/AlGaAs/GaAs/AlGaAs/GaAs heterostructure on a GaAs substrate, all direct bandgap materials and all not intentionally doped, typically obtained by epitaxial growth methods such as molecular beam epitaxy. The bottom serves as the growth layer after the

substrate, the top GaAs works as a protective layer, (typically a few tens of nm) to prevent the AlGaAs from oxidizing. The AlGaAs layers surrounding the central GaAs active region were assumed to have an aluminum content of 20 %. The role of the AlGaAs layer is twofold: first, avoid accumulation of charges and increase the current injection of our nanoLED (not studied here), and second increase the index contrast enabling better optical confinement in the active GaAs material.

2) **Dielectric region**: in these studies, silicon nitride with a refractive index of 1.45 was used. The role of the dielectric is two-fold: isolates the semiconductor from the metal, and in the case of a thick dielectric layer (>>10 nm), the losses from the metal layer can be substantially reduced;

3) **Mettalic region**: in these studies, silver coating was used. The metal helps to further confine light in the semiconductor active region with sub-micrometer sizes enabling the respective increase in the spontaneous emission (Purcell factor). Although the metallic cladding provides high reflectivity, it also contributes to the intra-cavity losses due to metal absorption. As mentioned in 2), a thick dielectric can mitigate this effect.

Differently from other cavities, such as Fabry-Perot cavities with 2D confinement, the optical cavity analyzed here has a complex 3D confinement meaning that no separation between longitudinal and transverse directions can be made, which leads to modes with all three polarization components. This makes more challenging the design of optical cavities and methods such as 3D FDTD (discussed next) are typical needed to obtain the relevant characteristics of metallo-dielectric cavities. In this work, cavity sizes from 350 nm to 1100 nm were simulated (this considers the width of the semiconductor only, see Section 3) and their respective emission properties (e.g. mode profile, resonant wavelength, quality factor, etc.) were analyzed in detail.

2.3 Finite difference time domain (FDTD) analysis

For the situation where the feature sizes of the structures analyzed (such as the metallo-dielectric structures analyzed here) are on the order of a wavelength, finite difference time domain (FDTD) solutions are required. FDTD is a state-of-the-art method for solving Maxwell's curl equations in the time domain, that is, it solves for *E(t)* and *H(t)*, which are the electric and magnetic, respectively, time-varying fields. It's also possible to obtain frequency results by using the Fourier transform.

The FDTD solves Maxwell's equations on a spatial and temporal grid like the Yee unit cell. The electric and magnetic fields are obtained with half of time step of difference meaning, that they are calculated at different times in the simulation. Depending on the dimension of the grid used this simulation can be extremely time consuming.

Considering the complexity of the nanocavity presented in **Figure 5**, 3D FDTD simulations are usually employed to obtain its relevant properties such as cavity quality factor and resonant wavelength. Therefore, in this work, in the FDTD simulations we used a 3D FDTD method based on Yee's cell algorithm with a perfectly matched layer (PML) boundary condition. The PML boundaries were kept at least half a wavelength away from the structure in order to not absorb radiation. We assumed an identical structure as the one shown in **Figure 5** where a single dipole source or a cloud of dipoles (with a Gaussian shape) is positioned in the GaAs region. In the simulations a mesh size (grid) of 20 nm and a mesh override of 17 nm in the active region was used. To simulate the emission of the GaAs a single dipole (with a gaussian shape) is positioned in the GaAs active region with either z, y or x using a broad band dipole to excite all the resonant frequencies in the cavity. After positioning the emitter in order to excite the mode inside the cavity, during the time domain simulation, the electromagnetic field is monitored in a number of points in the cavity. For this purpose, various monitors are used to acquire data, i) 3D profile monitor to analyze the electrical field distribution, ii) mode volume analysis to obtain the mode volume, iii) low and high Q analysis to obtain the spectrum and quality factor and, iv) an index monitor was used to obtain a plot with the refractive index of the various materials to make sure the structure simulated was the desired one, **Figure 6**.

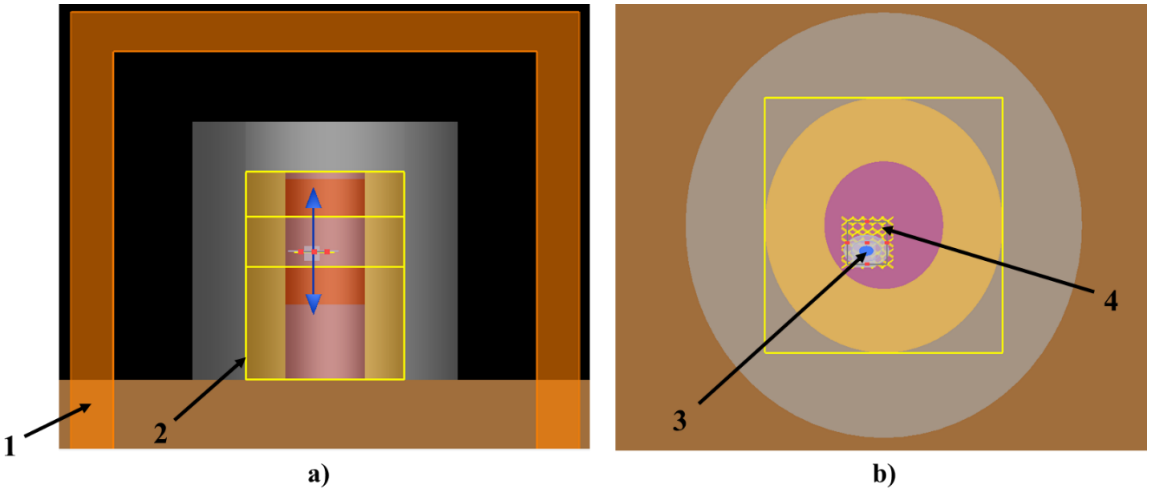

Figure 6 – Design panel in the LUMERICAL 3D FDTD software with a nanopillar simulation example, a) showing the xz view and b) showing xy view. The indicated numbers show 1- the simulation region in orange, 2- one of the several power/index monitors that was used (yellow line), 3- the position of the electric dipole and 4- the spectrum/ Q-factor monitors

2.4 Experimental methods

Fabrication

In this thesis, samples of micro- and nanopillar undoped AlGaAs/GaAs/AlGaAs semiconductor structures were characterized, as obtained from Dr. Bruno Romeira, who developed and carried out the nanofabrication process, while the e-beam lithography was realized by Dr. Jérôme Borme.[1] The main objective was to study the optical emission of the semiconductor pillars. Since for this characterization optically pumping of the pillars was needed, these pillars were fabricated without the metal coating. To obtain the final micro- and nanopillars desired several nanofabrication steps were performed. The steps included plasma enhanced chemical vapor deposition (PECVD)to deposit a SiOx dielectric material (used as a hard mask) followed by spin coating of e-beam using a resist track. The structures were patterned in the photoresist using a VISTEC 5200 ES 100kV Electron Beam Lithography tool. To finalize the fabrication the dielectric and semiconductor were etched using SPTS oxide etcher and SPTS ICP, respectively, and the dielectric hardmask was removed using vapor HF. For inspection of the samples, either an optical microscope or a scanning electron microscope (SEM) tool were used.

Microphotoluminescence setup

Confocal microscopy is an optical imaging sample- or laser-scanning microscopy technique for increasing optical resolution and contrast of a micrograph by means of using a spatial pinhole to block out-of-focus light in image formation. The confocal principle in laser scanning microscopy is as follows: coherent light emitted by the laser system (excitation source) passes through a pinhole aperture that is situated in a conjugate plane (confocal) with a scanning point on the sample and a second pinhole aperture positioned in front of the detector. As the laser is reflected by a dichromatic mirror and scanned across the sample in a defined focal plane, secondary fluorescence emitted from points on the sample (in the same focal plane) pass back through the dichromatic mirror and are focused as a confocal point at the detector pinhole aperture. In this work, a confocal microscope (LSM780, Zeiss) was used to

[1] During the master thesis, I had the opportunity to follow closely the nanofabrication process of the samples used in this thesis in the clean room facilities of INL.

acquire images of luminescent from fabricated semiconductor micro- and nanopillars. It consists of an inverted confocal laser scanning optical microscope providing excitation laser sources with wavelengths at 458 nm, 488 nm and 514 nm (Argon Laser) and 405 nm, 561 nm and 633 nm (diode laser). Regarding the objectives, it allows the users to use 10× and 20× air objectives, 40× both oil and water immersion objectives, and 60x oil immersion objectives. In this thesis, the excitation source used was the 561 nm diode laser, and for collection of the photoluminescence air objectives of 10x and 20x were used.

Time resolved photoluminescence setup

Time correlated single photon counting (TCSPC) is a technique based on the repetitive, precisely registration of single photons, e.g. from a luminescent signal. The sample is excited periodically using for example a pulsed laser source. The reference for the timing is the excitation pulse repetition rate. A single photon condition must be met to ensure that only one photon is emitted at maximum, having some cycles with no photon emissions [28]. Using this method, a histogram of photon arrivals per time bin is built to measure fluorescence decay profile curve of the signal. **Figure 7** illustrates how the histogram is formed over multiple cycles. It is also important to characterize the overall timing precision of the TCSP system, referred to the instrument response function (IRF). The excitation pulse detectors, and electronics, they all contribute to the broadening of the IRF, and therefore a deviation from the ideal case of an infinitely narrow IRF.

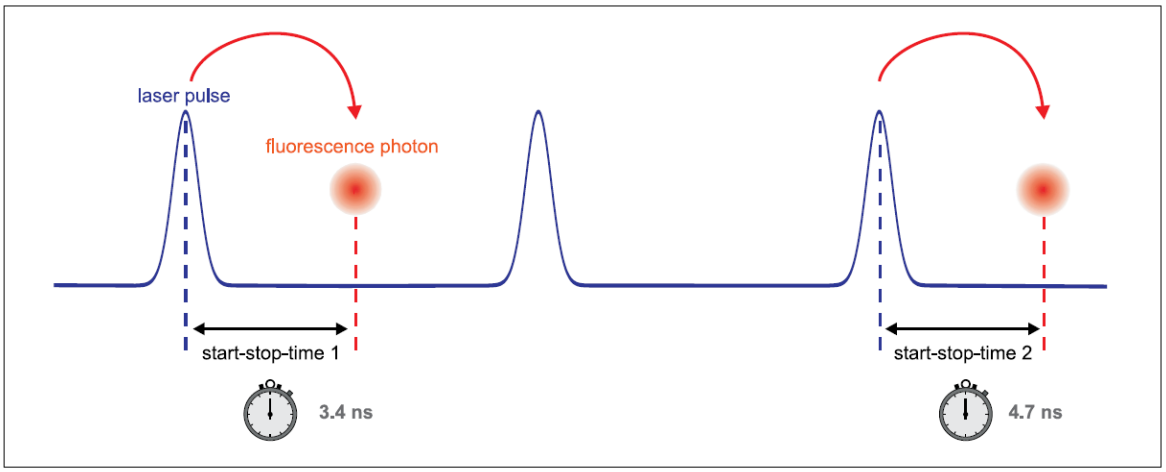

Figure 7 - Measurement of start-stop times in time-resolved fluorescence measurement with TCSPC (adopted from [28])

To study further the emission properties of the pillars, a fluorescence lifetime imaging microscopy (FLIM)system was used, **Figure 8**. It is a custom built- setup at the Ultrafast Bio- and Nanophotonics group, based on the TCSPC technique. A 561 nm picosecond pulsed laser with a repetition rate of 20 MHz was used in a confocal microscope setup equipped with suited optical filters, namely a dichroic (561 nm Long Pass) and a 780 nm long pass filter in the detection path. The microscope objective used was an oil immersion 100×(CF FLUO, Nikon). The sync signal of the laser and the TTL output of the APD (MPD) detector are coupled to a correlation card (SPC130, Becker & Hick). The sample is scanned via a x-y nanopositioner (NanoLPS200, Mad City Labs). The instrument response function (IRF) was recorded on a region of the bulk sample (located far from the pillar structures) where a laser reflection leads to the detected signal. As for the fitting, two methods were used. First, for the individual pillar decay lifetime, the Origin 9.1 single exponential fit was used. As for the FLIM images, a custom Matlab toolbox developed by Ricardo Adão (member of the Ultrafast Bio- and Nanophotonics group) using a multi-exponential fit based on Enderlein 1997 was used [29].

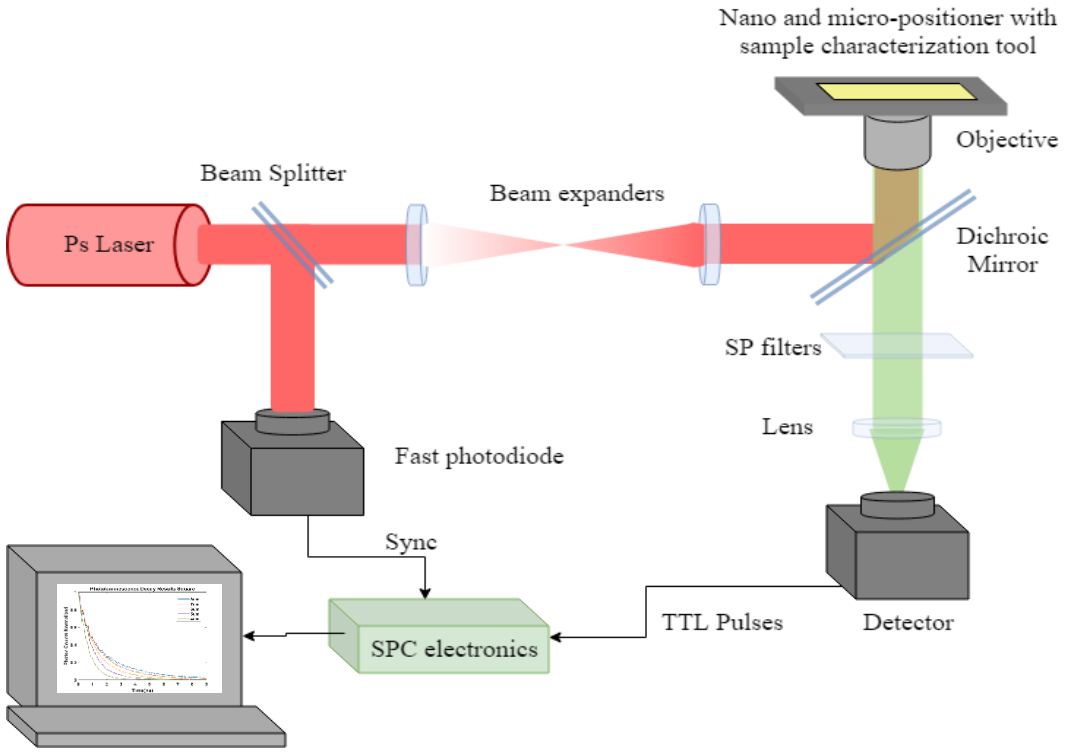

Figure 8 - Setup configuration of the Inverted FLIM Microscope used at the Ultrafast Bio- and Nanophotonics group.

In the time-resolved photoluminescence (TRPL) experiments, semiconductor pillar structures were optically pumped using a picosecond pulsed laser at 561 nm and the emission was filtered and detected by an APD. The TRPL decay curves are fitted using a single exponential decay function to obtain the values of the carrier recombination lifetime. The measured photoluminescent decay time, τ_{PL}, is related to the radiative and non-radiative decay times:

$$\tau_{PL}^{-1} = \tau_r^{-1} + \tau_{nr}^{-1} \tag{8}$$

The surface recombination velocity can be estimated directly from the size-dependent measured carrier lifetimes in the low injection regime. The photoluminescent decay gives us approximately the surface recombination decay rate. Assuming that surface recombination is proportional to $\frac{4v_S A}{V_a}$ [17] where A is the surface area, V_a is the volume of the active region and v_S is the surface recombination velocity, we have:

$$\frac{1}{\tau_{PL}} = \frac{1}{\tau_B} + \frac{4v_S A}{V_a}\ [17] \tag{9}$$

Where τ_B is the lifetime in the bulk. For samples were the active layer thickness is sufficiently small, the surface lifetime will dominate the recombination. We note this does not take into account other effects such as photon recycling [30].

Since the TRPL technique is very sensitive, and lifetimes at very low injection levels may be measured, the TRPL technique provides detailed features of the exponential decay of pillar structures that contain many insights into the specific recombination mechanisms of nanopillar-based LED sources.

3. Results and Discussion

In this section the results for both theoretical and experimental analysis are presented. In the simulation part (section 3.1), 3-dimensional finite-difference time domain (3D-FDTD) simulations were employed to simulate the optical field distribution of metallo-dielectric nanopillar structures with a circular geometry, **Figure 5**, ranging from d_s=350 nm to d_s=1100 nm (where d_s is the semiconductor pillar diameter). The results of the optical field distribution, the Q-factor, resonance frequency, mode volume, and the role of the metal coating are presented. In the simulations, the impact of tilted pillars and the impact of the excitation dipole source are also investigated. As for the experimental part (section 3.2), both steady-state photoluminescence and time-resolved photoluminescence were used to study the optical emission properties and carrier dynamics of the fabricated semiconductor pillar samples. The measurements were used to estimate non-radiative behavior of the samples, namely the surface recombination velocity of the pillar structures. Finally, from the experimental and theoretical results achieved, the expected internal quantum efficiency (IQE) values of metallo-dielectric light-emitting structures are analyzed and the potential of these devices for the design of efficient nanoLED sources is discussed.

3.1Simulation of metallo-dielectric nanocavities

The important aspects of the properties of the metallo-dielectric cavities are the the quality factor and the mode profile. The quality factor gives information about the time that energy is stored inside a cavity, that is, the rate of energy loss relative to the stored energy of the resonator. On the other hand, the mode profile gives information on the spatial confinement of the stored electromagnetic field. Modes are solutions for the equation of light propagation (eigenmodes) that describe the transport of energy and information. In this work, the metallo-dielectric configuration allow us to confine TEM spatial modes inside the cavity, specifically in the active region, typically resembling the modes found in whispering gallery cavities [31]. Since we are working with sizes comparable to the wavelength, the boundaries of the nanopillar will impose a discrete number of eigenmodes [32].

We note that the calculations of the quality factor depend on whether the electromagnetic field fully decays or not by the end of the simulation. In order to find the resonant frequencies of the structure, a Fourier transform of the field over time from a time monitor is taken. If a cavity has a small quality factor (i.e. the field fully decays during the time of simulation), the time domain electromagnetic field is Fourier-transformed, and the resonant frequencies are calculated so that the calculation of the Q-factor is simply the resonant frequency divided by the full-width-half-maximum (FWHM):

$$Q = \frac{f_r}{FWHM}. \tag{10}$$

In the presence of a high-Q cavity where the field is not able to fully decay during the simulation time the quality factor is calculated using the slope of the envelop of the slow decaying field.

$$Q = -\frac{2\pi f_r \, log_{10}(e)}{2m} \tag{11}$$

where m is the slope.

Lastly, as mentioned in the sub-section 2.1.2, calculations of the mode volume using Eq. (7). For the calculations, the electromagnetic field intensity ($|E_x|^2+|E_y|^2+|E_z|^2$) and permittivity (real(n^2)) data are saved for each position and frequency. The mode value assumed as εE^2 is normalized for each frequency. Lastly, $\varepsilon E^2$is integrated over the defined volume. In what follows, calculations of the optical field distribution, Q-factor, mode volume, and resonance frequency as a function of the pillar diameter are shown.

Size-dependent resonance wavelength, quality-factor and mode volume

In the simulations the nanopillar structure shown in **Figure 5** is considered for variable diameters of semiconductor (d_s) while fixing the dielectric (d_{die}=150 nm) and the metal layers (d_m=200 nm) and assuming a thickness of GaAs active material of 200 nm. We note that the thickness of the dielectric layer was chosen to reduce the losses due to the metallic layer – the values between150-200 nm were found to be optimal values for the sizes of pillars analyzed here, that is giving the highest quality factors. In this simulation (**Figure 9**) a single dipole (600-1200 nm) was used and positioned in the active GaAs material, in order to excite the modes in the GaAs.

Figure 9 shows that for different sizes, our cavity supports different mode profiles where a large portion of the spontaneous emitted light is funneled to a single mode with a relatively narrow spectral range, a case very difference from large-scale LEDs where light is emitted in a broadband spectral region. In the cases analyzed, the electric field of the modes is guided close to the circumference of the cylinder's cross-section, analogous to whispering gallery modes in micro disk cavities. Therefore, the electromagnetic energy is mostly confined in the GaAs high index region, instead of propagating in a certain direction. It is important to stress that the nature of the light-metal interaction is distinctly different than a purely plasmonic interaction. In a surface plasmon, electric field lines are terminated on the metal surface where charge accumulates. In the case shown in **Figure 9**, electric field lines are parallel to the metal surface and are thus repelled from the metal itself. This reduces the amount of electromagnetic energy in the metal and increases the optical quality factor of the metallo-dielectric nanocavity. As shown in **Figure 9**, this metallo-dielectric structure can operate at wavelengths ranging from ~800 nm up to 1200 nm, depending on the cavity size. We can also observe that for each mode we have approximately a linear increase between diameter and wavelength. This linear increase is slightly larger for smaller diameter sizes.

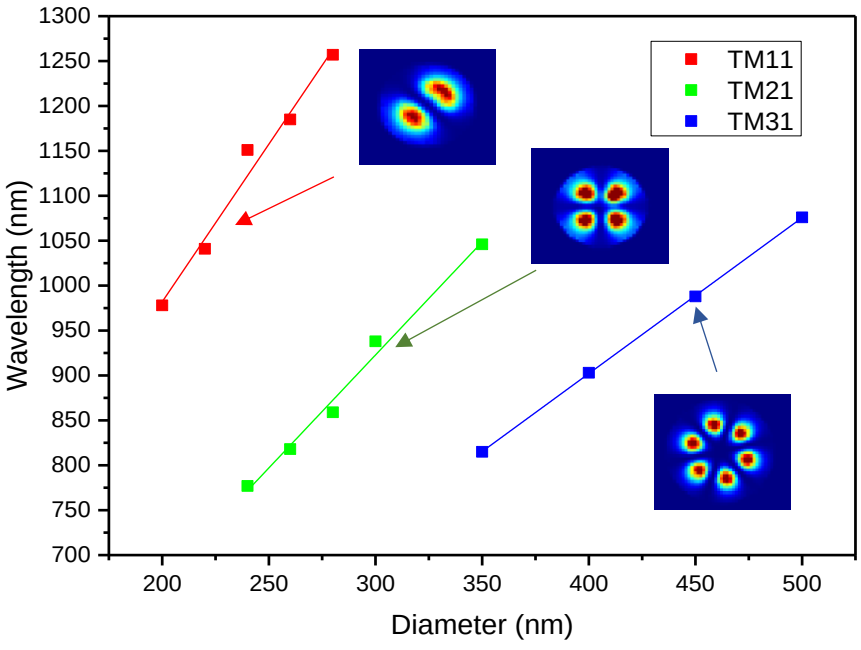

Figure 9 - Peak wavelength for various diameters for three different modes for a metallo-dielectric cavity with a 200 nm metal capping layer. A linear fit is plotted for the different modes showing the following wavelength sensitivity to the cavity size: TM_{11} - 35.1 nm (λ)/10 nm (d); TM_{21} - 25.2 nm (λ) /10 nm (d); TM_{31} – 17.42 nm (λ) / 10 nm (d).

Considering the complex metallo-dielectric structures a general method to obtain the cavity quality factor consists in placing a number of electric or magnetic dipoles inside the cavity with random positions, orientations (i.e. polarization), and phase, which excite all possible modes inside the metallo-dielectric cavity. In what follows the simulations results of the quality factor and mode volume as a function of diameter are shown using a cloud of dipoles (15) randomly positioned across the active region, this time, with a wavelength of 700-1000 nm. These new values were chosen to be in accordance with the emission of the GaAs. The values of quality factor and mode volume are plotted in **Figure 10**. The value of the mode volume was taken at the peak of the resonance wavelength.

In the results of **Figure 10** we note that the pillars above 1 µm we achieve quality factors close to 2000 while for the smaller pillars ~300 nm the quality factor is reduced to values <250. This is expected since as the cavity is shrunk and approaches the diffraction limit, large amounts of energy escape the high-index semiconductor as radiation. Regarding the results of the mode volume in **Figure 10**, the mode volume is reduced almost 10-fold when the cavity is reduced form 11000 nm to 300 nm. We note that for the smaller cavities the mode volume $V < V_a$ (where V_a is the volume of active region) while for larger pillars the mode size is comparable to the volume of the active region. This is a key result since, as explained in Section 2.1, Eq. (6), the spontaneous emission rate can be modified via the mode volume parameter so that a large Purcell enhancement of the spontaneous emission can be achieved, $F_P \propto \frac{1}{V}$.

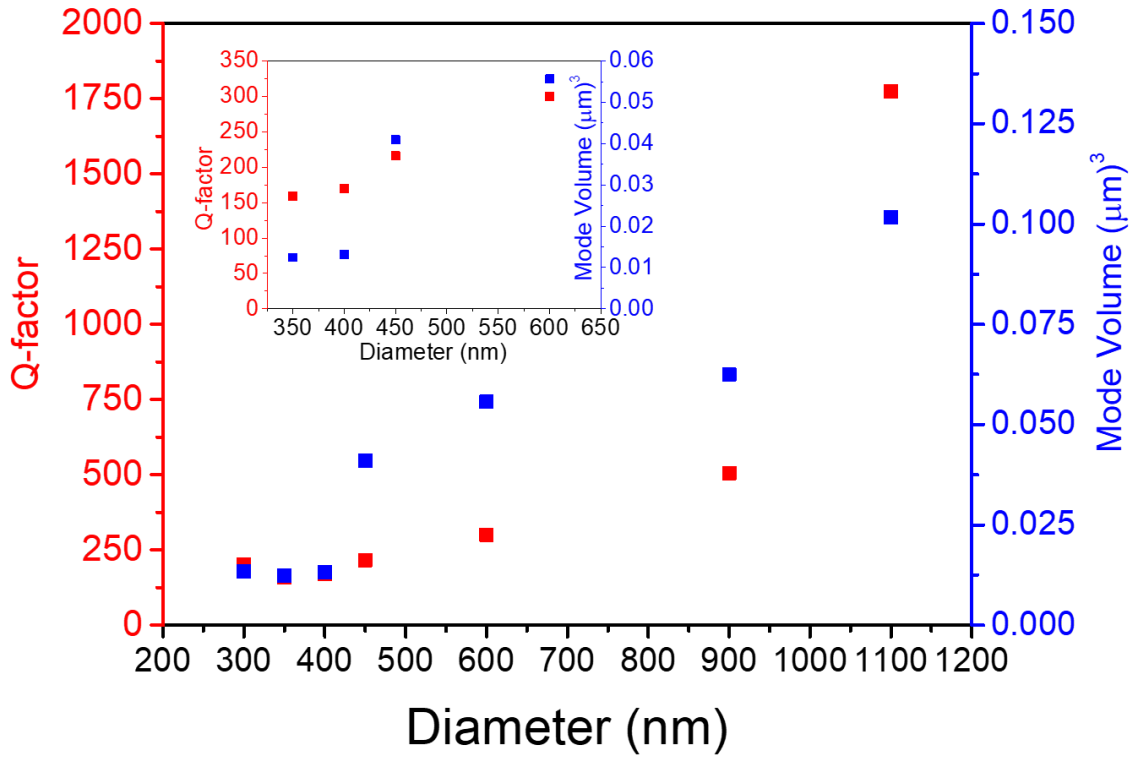

Figure 10 – Simulations of the quality factor and mode volume for a device with 200 nm active region as a function of diameter size in the presence of a 200 nm layer of metal using a cloud of dipole as a source of excitation, Inset is shown the results for the smaller pillars.

Role of the metal

In order to understand the role of the metal in metallo-dielectric cavities, a simulation of the nanopillar in the same conditions as **Figure 10** was made to compare both situations of a cavity with and without metal capping. **Figure 11** shows the electromagnetic energy for a 400 nm diameter semiconductor pillar with and without metal layer. The thickness of the metal layer used was 200 nm in **Figure 12**, the Q-factor values for the case of a thick and thin metal layer are plotted. The Q-factor for the pillar without the metal layer is not shown since for these very small cavities it was not possible to obtain a clear resonance peak to due to the large radiation losses of the small pillars

In **Figure 11** a) and c) we can see the XY view of the electromagnetic energy in the active region. In **Figure 11** b) and d) it is shown the corresponding XZ view. In the case where the metal capping is not used, **Figure 11**(a), (b), almost no confinement is achieved in the middle GaAs active region – see (b). Furthermore, a large portion of the evanescence electromagnetic field is now located in the dielectric and air regions, that is, outside the semiconductor region. However, when the metal layer is included, as seen in **Figure 11**(d), a large portion of the electromagnetic energy is now located inside the semiconductor region, namely in the GaAs active region. Also, the evanescence field is substantially reduced. Therefore, by carefully selecting the dielectric and metal layers, a good confinement of the electromagnetic energy can be achieved. Further vertical confinement could also be achieved by increasing, for example, the thickness of the cladding layers surrounding the active region material. This allow us also to optimize the extraction of light from the pillar since there is a tradeoff between tight confinement of light and out coupling efficiency. However, these studies were not part of the work presented here.

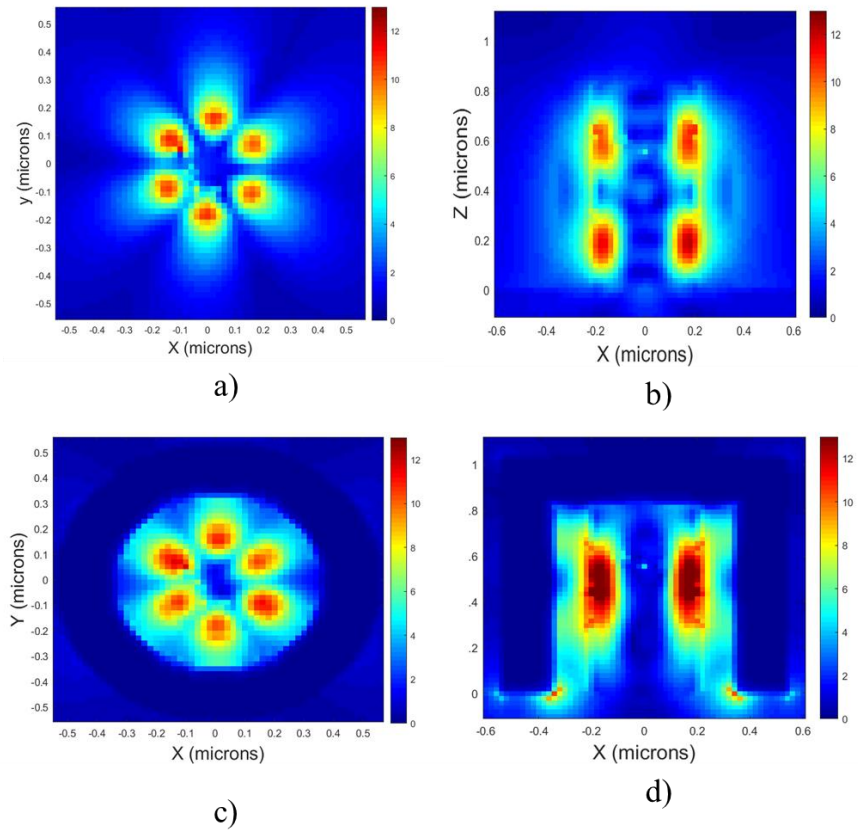

Figure 11 - Electric field distribution for a) and b) 400 nm pillar without metal layer, XY and XZ view, respectively, and c) and d) 400 nm diameter pillar with a 200 nm thick metal layer, XY and XZ view, respectively.

Figure 12 shows a comparison between the quality factor of a nanopillar capped with a 200 nm metal layer and a pillar with a 20 nm capped layer. The results are consistent with the **Figure 11** where we have increased light confinement for a thicker metallic layer. As stated, a large confinement improvement is achieved when carefully selecting both metal and dielectric layers.

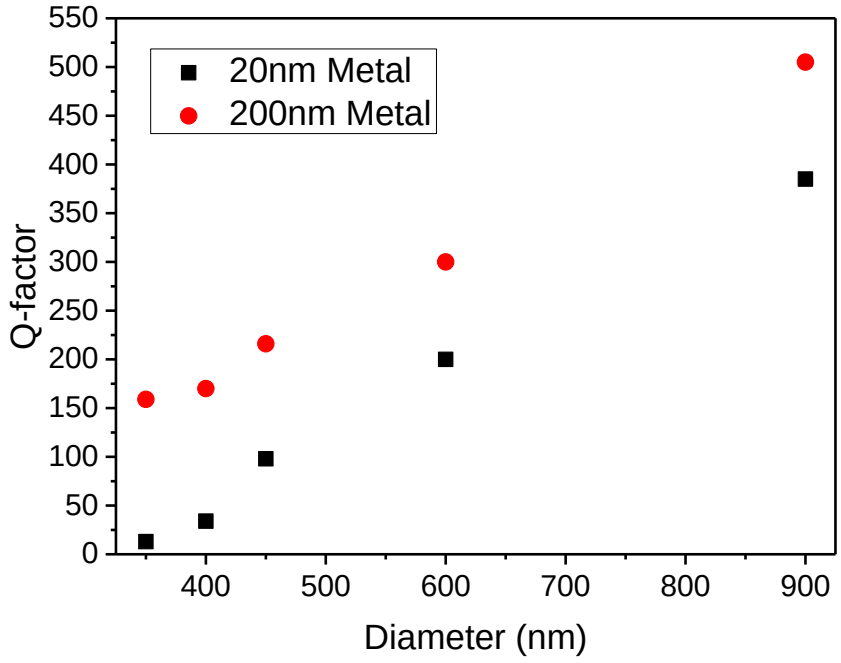

Figure 12 - Quality factor comparison between a nanopillar with 20 nm thick metal layer vs 200 nm thick layer.

Effect of the pillar sidewall angle

In the experimental results section 3.2 we will see that achieving perfectly vertical walls in the pillars is challenging from the point of view of fabrication. Instead, in many cases a pillar with tilted walls is obtained and so, a study regarding the Q-factor for the case of tilted walls was made. Its Q-factor was studied using an angle of 10º. **Figure 13** shows the electric field distribution for one example of the pillars studied. The result is compared with previous results using a perfect vertical sidewall. **Figure 13** shows the mode profile inside a 900 nm diameter tilted pillar. As we can see in **Figure 13** b) it is still possible to achieve some confinement in the active region but due to the tilted walls we end up having the mode spread across other parts of the pillar, namely in the dielectric. **Figure 13** a) shows the mode confined.

Figure 14 shows the quality factor results for both tilted and straight pillars. The results show clearly that the sloped walls affect the temporal confinement of the cavity (Q-factor). The results for pillar sizes between 300 to 400 nm are not shown. As we reach smaller sized pillars, it becomes more difficult to achieve mode confinement. By having smaller cavities with imperfections, it is even harder to confine the mode and so the monitor might not be able to calculate data. We also see that for larger sizes the difference in Q-factor between the straight and sloped pillars is smaller. This might mean that for larger pillars the imperfections are not so relevant.

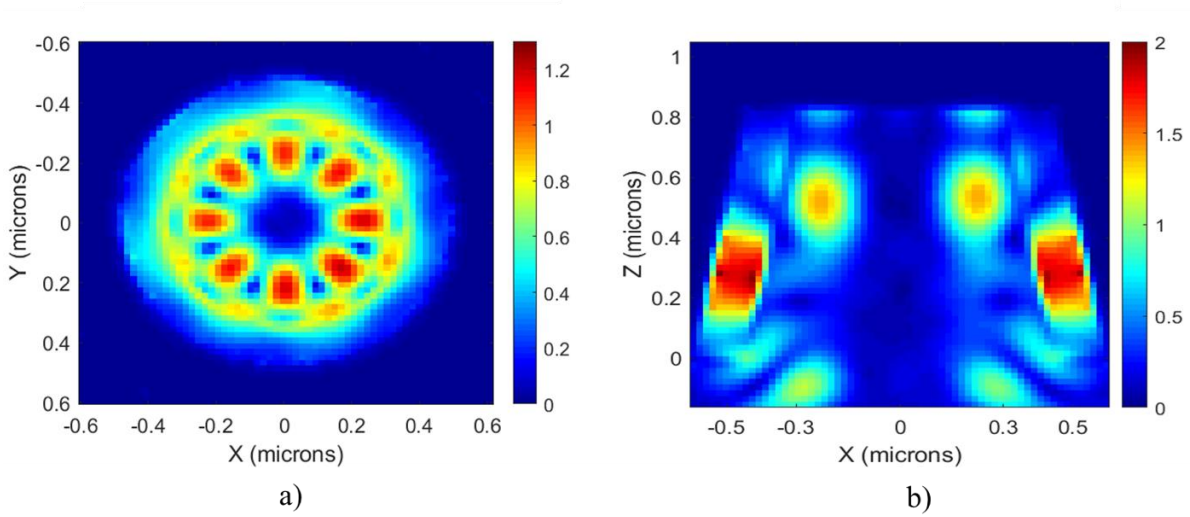

Figure 13 – Electric field distribution $|E|^2$ inside a 900 nm diameter pillar with an angle of 10º a) XY view and b) ZX view.

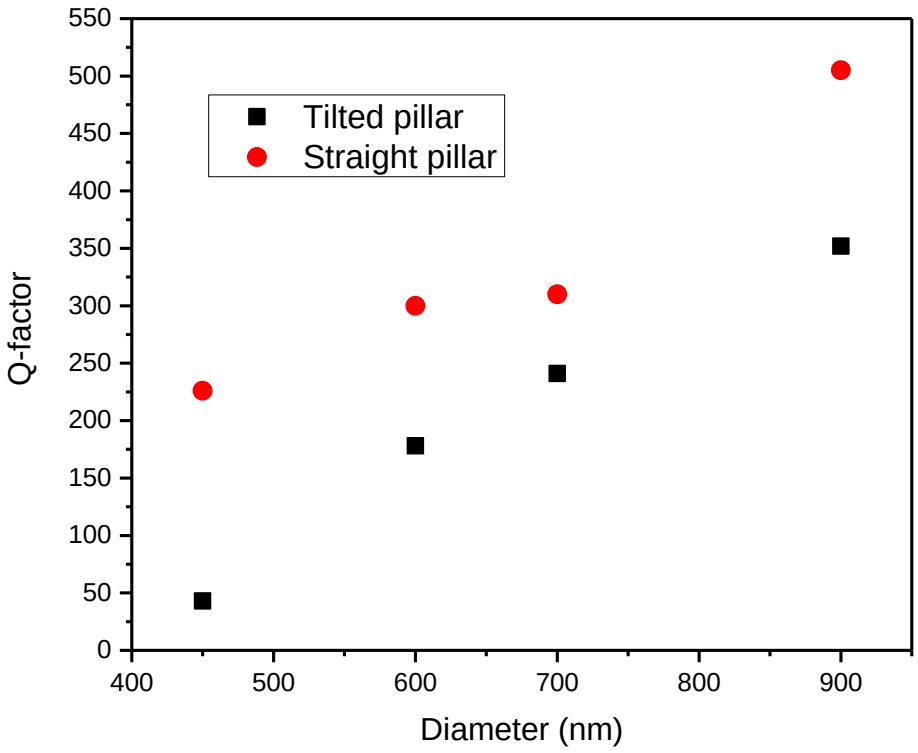

Figure 14 – Comparison of the Q-factor results for a 10º tilted pillar and for a straight pillar.

Impact of the position and orientation of the excitation dipole

Depending on the objective of the simulations, either, a single dipole or a cloud of dipoles was used. In order to study all the possible modes that can be excited inside a nanocavity, one should simulate one dipole in several positions for the entire simulating region. Due to lack of a dedicated CPU only one simulation per dipole/cloud of dipoles was usually used since this approach is much less time consuming and already give us accurate results if the position of the dipoles is chosen carefully. This section aims to show that depending on the position chosen the user might get different results by simulating a single dipole changing both orientation (x, y and z) and position (center of the pillar and edge of the pillar). In this analysis, one shows the obtained emission spectrum for each simulated dipole, **Figure 15**. The nanopillar simulated had the following structure: bottom GaAs (300 nm), bottom and top AlGaAs (150 nm), AR (200 nm), top GaAs (30 nm), dielectric (150 nm), metal (200 nm), and using a diameter of the semiconductor pillar of 300 nm. In this simulation, a single electrical dipole with wavelength 700-1000 nm was used.

Figure 15 show the spectrum intensity result for the 2 dipoles with different orientations studied. Dipole 1 is placed in the center of the pillar and dipole 2 is placed in the edge of the pillar. The respective letter stands for the orientation. Focusing on the dipoles 1,2, (x and y oriented) we can see that the peak frequency (λ=885 nm) is the same, the Q-factor is around 200 and the intensity is fairly close meaning that for the same position the XY orientation provides similar results. However, for z-oriented dipole, the position is of key importance since vertical polarized dipoles can easily excite the typical TM modes found in these cavities. Dipole 2-Z shows a smaller intensity when compared with Dipoles 1-X and Y and Dipole 2 – X and Y, but we still have the same peak frequency. The inset shows the Dipole 1-Z showing a lower intensity and a shift to right on the peak frequency. When testing a Z dipole in an optimal coupling position we get the same results as before (Q=200 and λ=885 nm) while for the center position, we obtained Q=30 and λ=905 nm. Different pillar sizes were tested (not shown) revealing similar results as the ones presented here. The results are consistent with the types of mode profiles typically found in these nanocavities which typically contain a low intensity field in the center of the cavity and a high intensity filed in the region close to the circumference of the pillar.

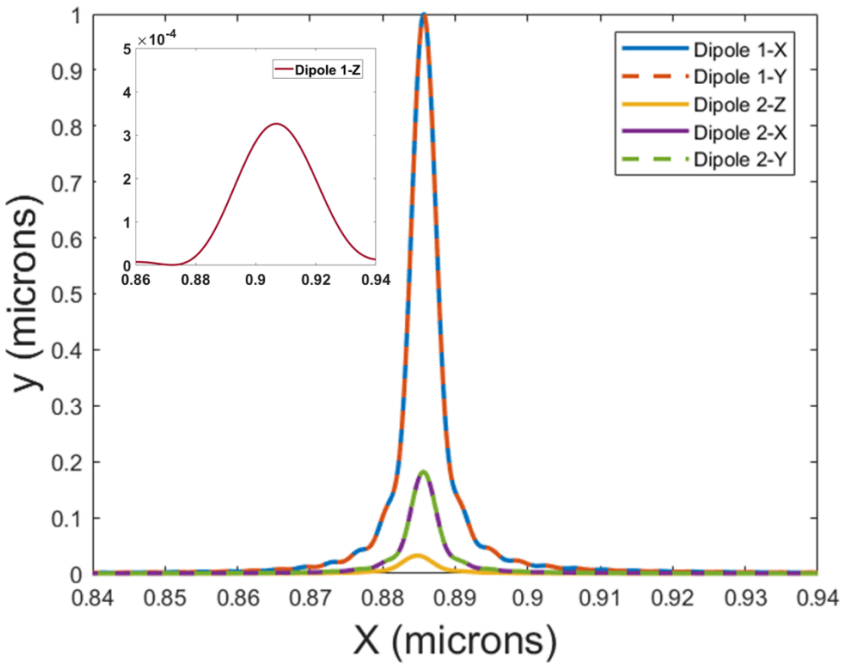

Figure 15 - Spectrum obtained for the 3 orientations and 2 positions tested. Dipole 1 is placed in the center of the pillar and dipole 2 is placed in the edge of the pillar. The respective letter stands for the orientation.

In this section we analyzed the resonance wavelength, quality-factor and mode volume of the metallo-dielectric cavities. The effect of the metal and tilted pillars in the quality-factor of the cavities was also studied. These analyses allow us to conclude the benefits of adding a cavity in terms of Q-factor and light confinement when the size of the structures is well below 1 micrometer by carefully selecting the thickness of the cladding metal-dielectric layers. Further simulations for optimization would include the study of the dielectric layer (thickness), study of the metal not just the presence but rather the effect for different thicknesses, and changing the cladding AlGaAs semiconductor layer, either its size or material, to achieve an optimal confinement.

3.2 Characterization of nanofabricated pillars

In this section, a brief overview of the samples of micro- and nanopillar undoped AlGaAs/GaAs/AlGaAs semiconductor structures with circular and square geometries is given. The micro- and nanopillars were fabricated on a 20 mm samples from a wafer of undoped AlGaAs/GaAs/AlGaAs material. The layer stack was composed from top to bottom by 150 nm of AlGaAs, ~50 nm of GaAs and, 150 nm of AlGaAs, and 300 nm GaAs all not intentionally doped, grown on an GaAs substrate grown by Molecular Beam Epitaxy (MBE). The main objective was to study the optical emission of the semiconductor pillars. Since for this characterization optically pumping of the pillars was needed, these pillars were fabricated without the metal coating. The nanofabrication was developed and carried out at INL cleanroom facilities by Dr. Bruno Romeira while the e-beam lithography was realized by Dr. Jérôme Borme.

Figure 16 shows the e-beam mask used to pattern the e-beam resist using the electron beam lithography tool.

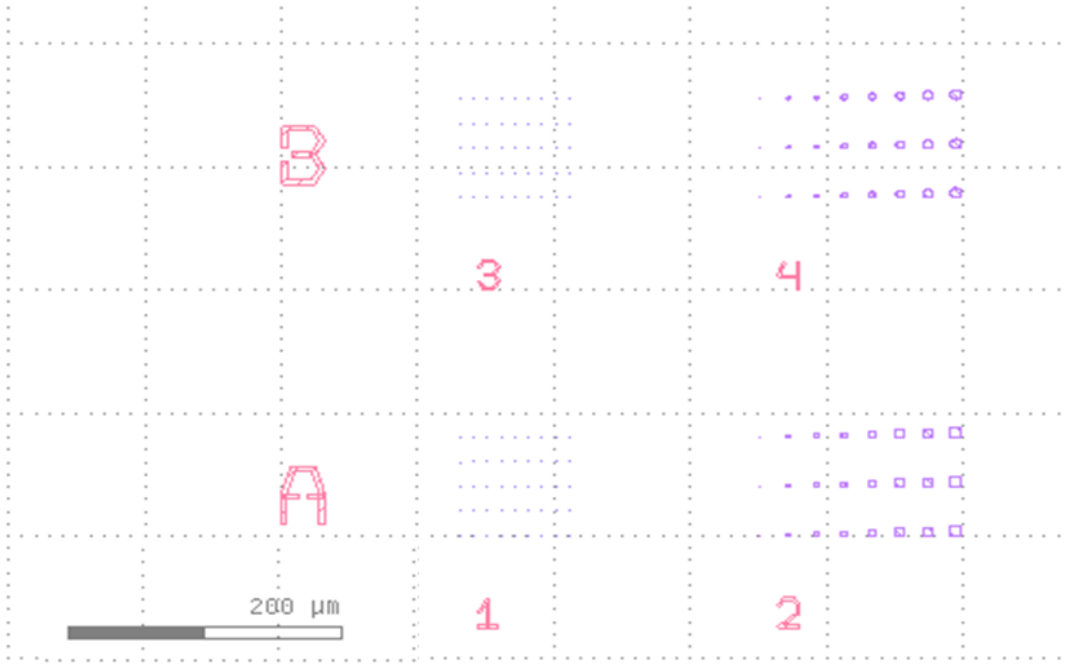

Figure 16 - Nano and micropillar structures layout mask. In section A1 are displayed the nanopillars with a square geometry ranging from 200 nm to 1 µm width. Section A2 shows the square micropillars ranging from 1 µm to 8 µm. Sections B3 and B4 show the nanopillar and micropillar structures, respectively, with identical dimensions as the square pillars.

Figure 17 shows the optical microscope images from the nanopillars obtained after e-beam exposure and photoresist development using the layout masks shown in the **Figure 16**. The dose used in the e-

beam was previously optimized by Dr. Bruno Romeira in order to not cause an overexposure in pillars with close proximity.

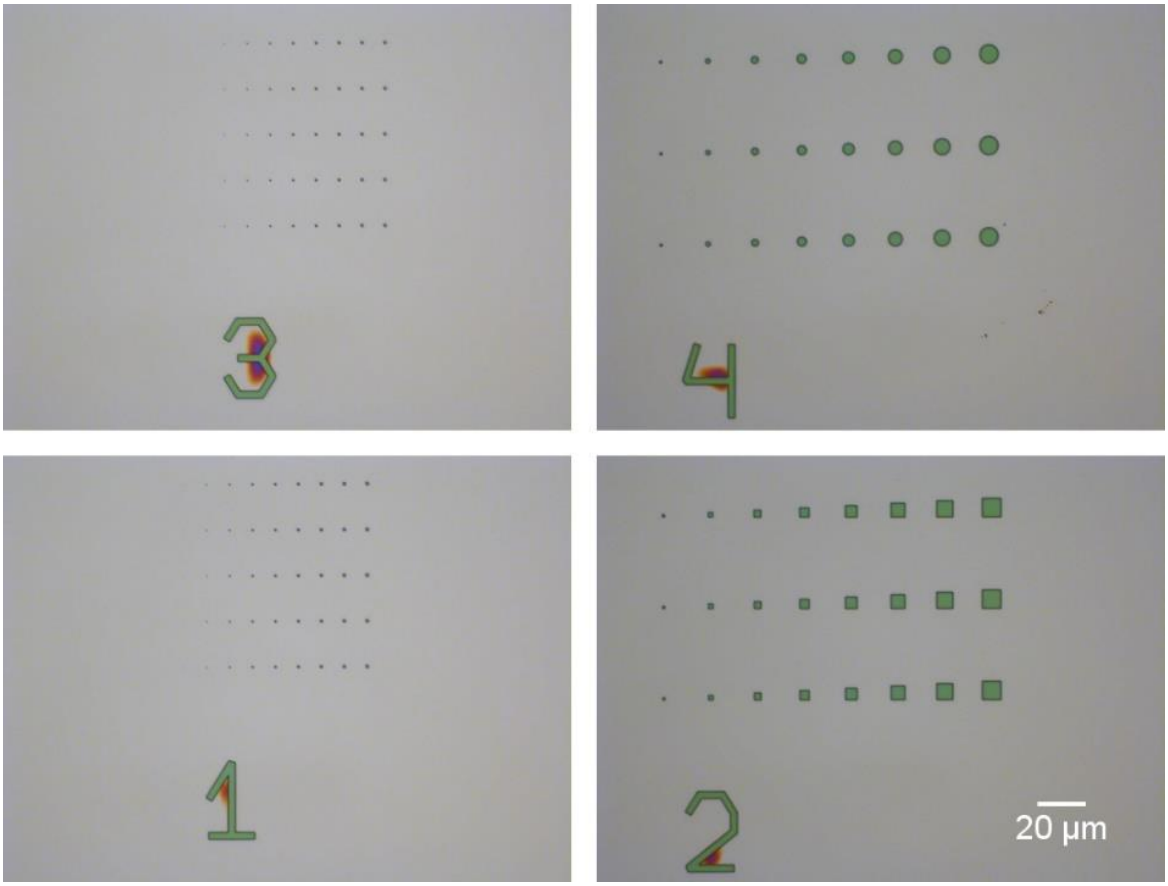

Figure 17 - Optical microscope images after e-beam exposure and photoresist development (nanopillars on the left, dose: 800 µC/cm^2) and (micropillars on the right, dose: 500 µC/cm^2). Image courtesy of Dr. Bruno Romeira.

Figure 18 shows the scanning electron microscope (SEM) images of both micro- and nanopillars, both squared (a-d) and circular (e-f) at different steps of production. The pillars shown below are just some examples of the pillars fabricated and characterized. Panel a) shows a top view of a squared pillar after e-beam exposure and e-beam resist development. Panel b) shows a tilted view after oxide etching showing both the e-beam resist on top (~500 nm) and the SiO_2 material (~200 nm). Panels c)-f) show examples of pillars after dry etching of the semiconductor using SPTS ICP tool. The typical etching thickness for the pillars studied here was around 0.6 µm. As clearly seen for the smaller pillars in c) and f), after etching the pillars show pronounced tilted walls, and for this reason, a study on the effect of the sidewall angle on the cavity optical performance was previously shown.

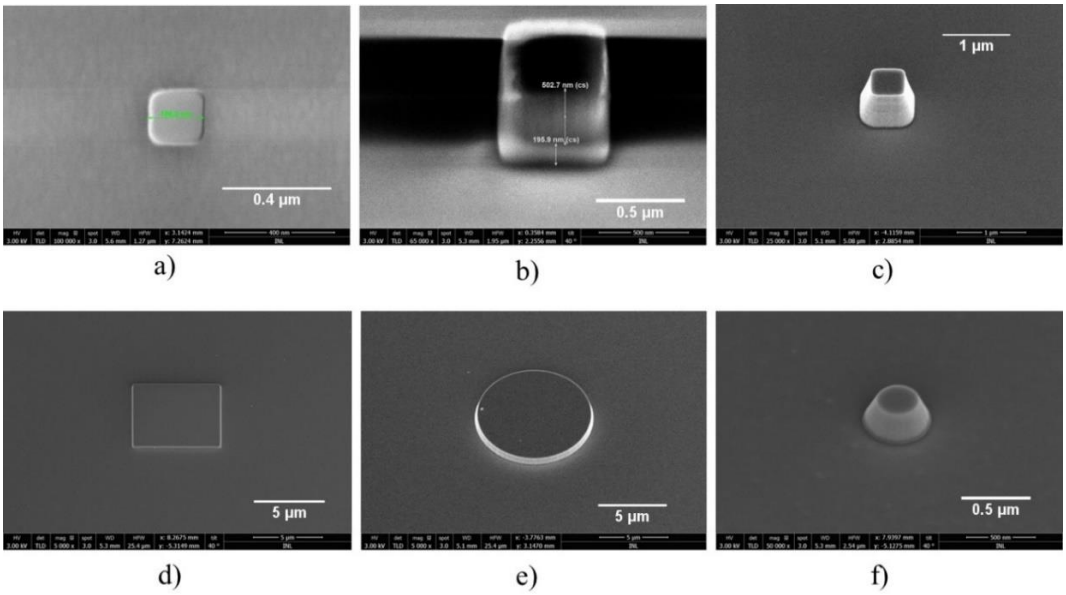

Figure 18 - SEM images a) 200 nm square nanopillar after e-beam exposure and photoresist exposure, b) Square pillar after oxide etching, c) 400 nm square nanopillar after semiconductor etching, d) 6 µm square micropillar after semiconductor etching, e) 8 µm circular micropillar after semiconductor etching and f) 200 nm circle nanopillar after semiconductor etching. Image courtesy of Dr. Bruno Romeira.

3.3 Microphotoluminescence from micro- and nanopillars

The confocal microscope was used to analyze the luminescence of both the micropillars and the nanopillars produced..**Figure 19** shows the continuous-wave photoluminescence measurement results at room-temperature displaying typical confocal microscopy images from micropillars (a) and nanopillars (b) for the case of squared pillars. Using **Figure 19** we were able to plot a graph with the intensity across the pillars. The outline color (red and blue) used in **Figure 19** was used to distinguish easily micropillar data (red outline) from nanopillar (blue outline).

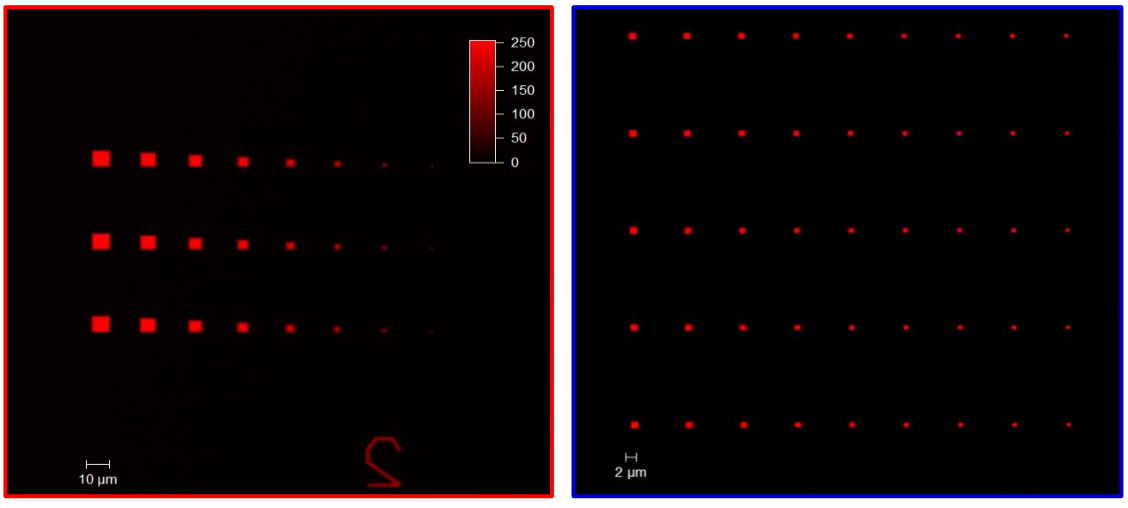

Figure 19 - Confocal image of a) squared micropillar array ranging from 8 µm - 1 µm and b) squared nanopillar ranging from 1 µm -200 nm.

Figure 20 shows the intensity profiles from the micropillars and nanopillars taken for the analysis of **Figure 19**. In **Figure 20** a) we can see that the intensity of light emitted from the micropillars with diameter, following a typical scaling area-law d^2, of planar light-emitting diodes. However, for the nanopillars shown in b) we see a maximum peak around 300 nm. When going down in size, the surface to volume ratio increases and it is expected that surface properties become more relevant. With this in mind, it is expected a drop in intensity with the size due to surface recombination effects and the decreasing area. This pronounced effect of emission increase for the nanopillars was previously observed and is currently under study in the Ultrafast Bio- and Nanophotonics group and the preliminary results were presented in [33]. The main reason for the strong enhancement of emission is related to an increase of the light extraction efficiency for the smaller pillars. Since this part of the work was not the scope of this thesis, we will not go in depth on this topic.

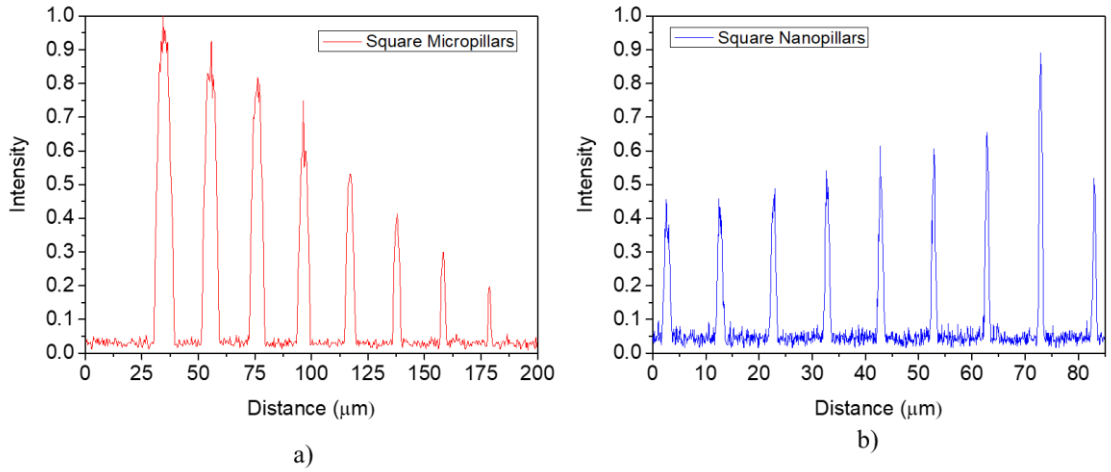

Figure 20 - Intensity profile normalized to the maximum intensity across a) square micropillars ranging from 8 μm - 1 μm and b) square nanopillars ranging from 1 μm - 200 nm from left to right.

3.4 Time resolved photoluminescence from micropillars

As described in section 2.4, a time-correlated single photon counting technique was used to study the optical properties of the pillars. This section will show a study on the carrier lifetimes of the micro pillars estimated from the measured time-resolved PL decay curves. Since as described in Section 2.4 the measured decay curves which scales as $\frac{d}{4v_s}$, the respective values of surface recombination were extracted for each measured pillar allowing us to estimate the internal quantum efficiency of these structures.

Figure 21 (a) and (c) shows a spatial distribution of photon counts for the case of a selected 8 μm and 6 μm squared micropillar, respectively (in the appendix section, **Figure 25**, is shown a full scan of the pillars analyzed here). Each pixel corresponds to the intensity of a decay curve that is extracted and used to obtain **Figure 21** (b) and (d) which is the corresponding lifetime for that pixel. As explained in the materials and methods section, **Figure 21** (b) and (d) are obtained using a Matlab toolbox using a multi-exponential fit with a modelled IRF.

In **Figure 21** (b) and (d) we can see that the lifetimes values in the center of the pillar are larger than the ones obtained close to the surface of the pillars. This give us information about the recombination processes that occur in the pillars. Clearly, near the surface the non-radiative effects such as surface recombination has a larger impact than in the center of the pillar resulting in much shorter lifetimes. Moreover, it is expected that the surface recombination effect has a greater impact on the smaller pillars due to the large surface to volume ratio, and therefore shorter lifetimes.

Using ImageJ, we can estimate the percentage area that irradiates with a fluorescence lifetime > 2ns for **Figure 21** (b) (around 44%). It was calculated that a considerable area of the pillar, around 56%, is affected by surface recombination. As for **Figure 21** (d) using again the ImageJ we achieve a region with lifetime > 1.1ns for only 34% of the total area of the pillar.

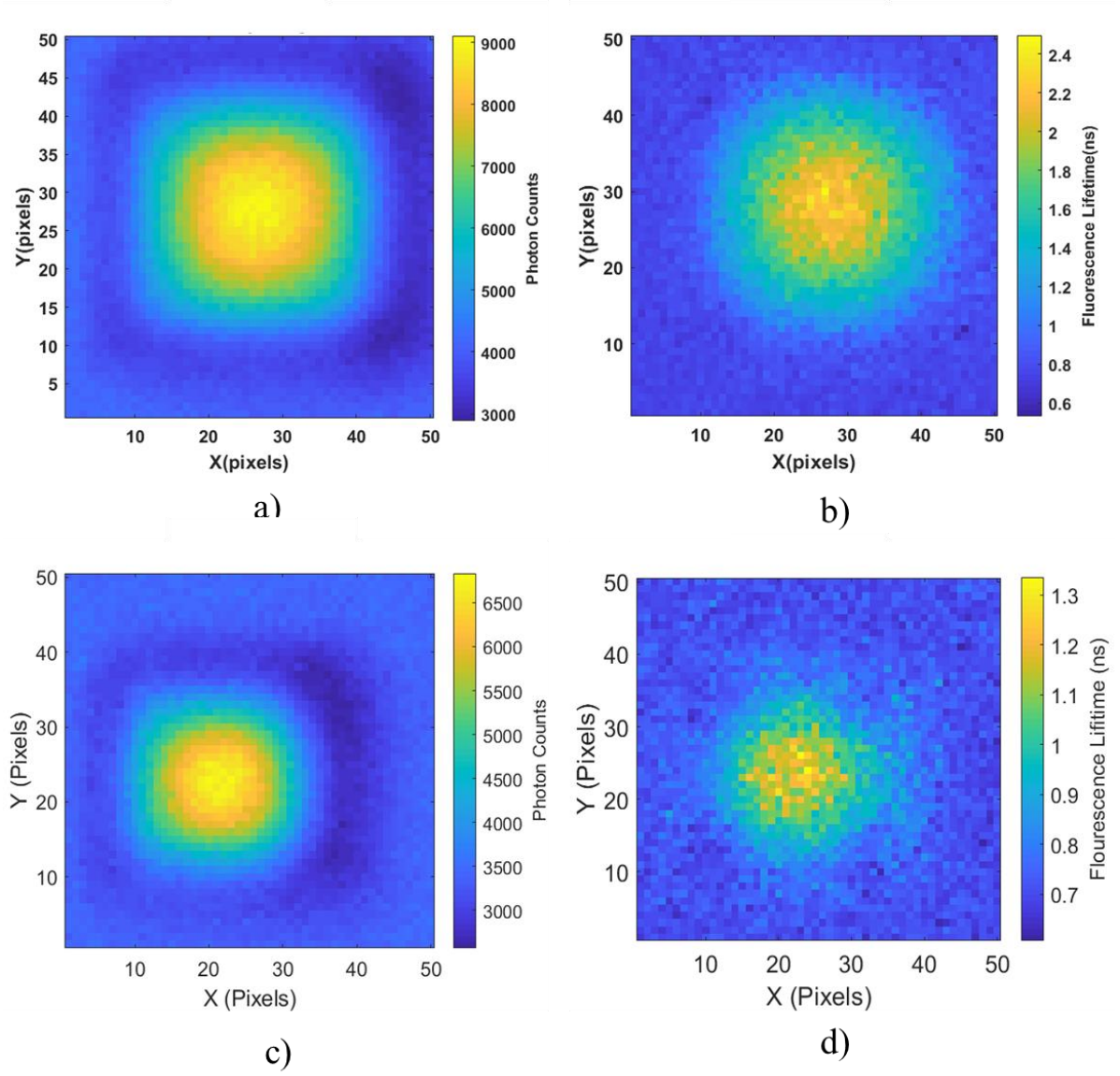

Figure 21 – Intensity image of a) an 8 µm micropillar and c)a 6 µm micropillar obtained using the FLIM setup and the respective fluorescence lifetime image under a pulsed 561 nm laser, b) 8 µm micropillar and d) 6 µm micropillar.

Figure 22 presents the photoluminescent decay curves for both squared and circle nanopillars ranging from 8 µm to 4 µm with both linear and logarithmic scale. **Figure 22** b) and d) shows the intensity in logarithmic scale and showing that the decay curves have approximately a single exponential decay. Using OriginLab the curves presented were fitted using a single decay exponential and the lifetime result (τ) was obtained for each size. Since the lifetime s analyzed here were considerably larger than the IRF, the deconvolution between the signal and IRF was not performed in this analysis.

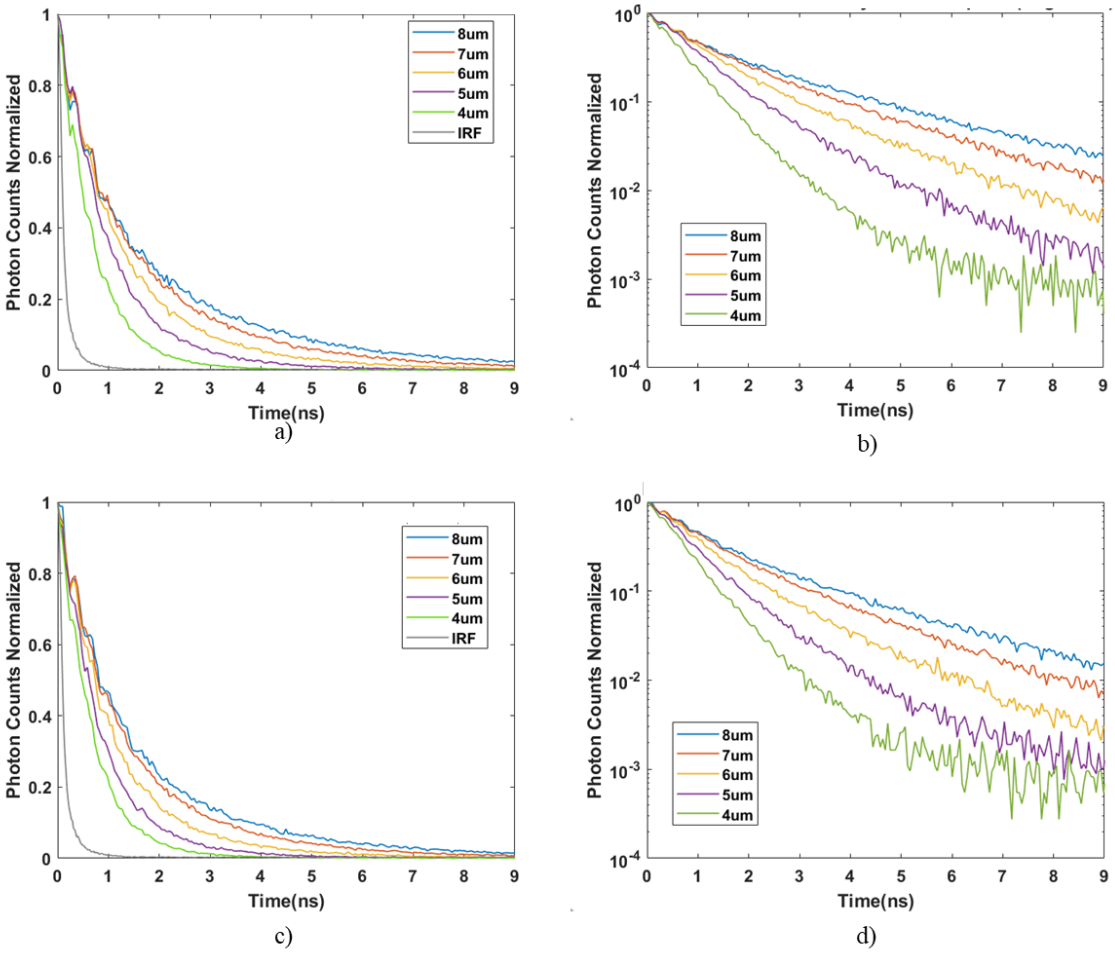

Figure 22 - Photoluminescence decay curves extracted from pixels in the FLIM images for a) and b) Squared micropillars with linear and log scale, respectively, and c), d) Circled micropillars for linear and log scale, respectively.

3.5 Determination of the surface recombination velocity

Figure 23 shows a lifetime *vs size* plot with the photoluminescence lifetimes extracted from the measured TRPL curves shown in **Figure 22** and fitted with a single exponential decay function . Using equation (9) we can obtain the surface recombination velocity value for each measured pillar. **Table 1** shows the results of the surface recombination obtained for each pillar analyzed. The surface recombination velocity values for the pillars with identical sizes are identical and do not vary substantially with the size of the pillar. The obtained values are comparable with the results obtained in [17] for non-passivated structures. For the calculations of the IQE shown next we assumed the best-case scenario of the surface recombination obtained for the 8 µm pillar with a surface recombination of 7.50×10^4 cm/s.

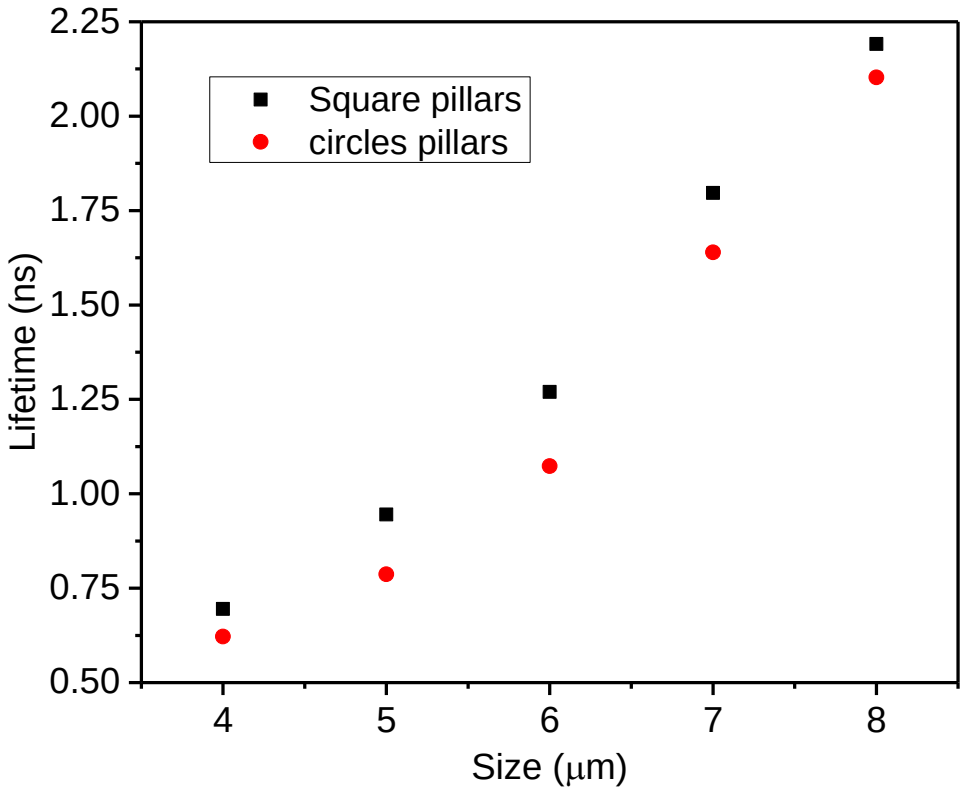

Figure 23 – Carrier recombination lifetimes versus diameter extracted from the measured TRPL curves fitted with a single exponential decay function.

Table 1- Surface recombination velocity results obtained for each pillar analyzed.

Surface Recombination cm/s	8 μm	7 μm	6 μm	5 μm	4 μm
Squared pillars	7.50×10^4	8.35×10^4	1.06×10^5	1.22×10^5	1.36×10^5
Circle pillars	7.87×10^4	9.51×10^4	1.28×10^5	1.49×10^5	1.53×10^5

3.6 Determination of the internal quantum efficiency of metallo-dielectric micro- and nanopillars

One of the main objective of this master thesis is to estimate the values of IQE, equation (1), for metallo-dielectric cavities and analyze the potential of nanoLEDs as efficient light sources. By using the values shown in **Figure 23** the nonradiative recombination values as a function of the pillar size can be obtained. As mentioned, in this analysis the Auger recombination is neglected since it only has a role for large pumping conditions. In order to simplify the analysis, we have chosen a fixed value for the surface recombination velocity of 7.50×10^4 cm/s. For the calculations of the radiative recombination part, the values of spontaneous emission in the cavity were shown by solving equation (6) and using the mode volumes calculated in **Figure 10**. We note that here we assume that in the case of a metallo-dielectric cavity all the spontaneous emission is funneled to a single mode so that the value of the radiative recombination rate is approximately the same to the spontaneous emission rate in the cavity. Table 2 shows the typical parameters used to calculate the spontaneous

emission in the cavity. With both radiative and nonradiative recombination values we can solve equation (1) and plot the expected IQE values as a function of the size of the metallo-dielectric cavity.

Table 2 - Parameters used to calculate the spontaneous emission in the cavity.

Name	Symbol	Value	Units
Reduced Planck Constant	$\hbar$	1.054571×10^{-34}	J.s
Dipole momentum	d_{if}	1.309×10^{-56} [30]	C.m
Cavity peak emission	ω_{cav}	1.459	eV
Homogenous Broadening	$\Delta\omega_{em}$	32.9×10^{-3}	eV
GaAs permittivity	ε_r	3.5	-
Permittivity in vacuum	ε_o	8.85×10^{-12}	$F.\mathrm{m}^{-1}$

Figure 24 shows the calculated internal quantum efficiency for a semiconductor pillar with a metallo-dielectric cavity for sizes ranging from 0.35 μm to 1.1 μm as studied in section 3.1. Also shown is the spontaneous emission rate in the cavity. The results show that for smaller sizes the internal quantum efficiency can be as high as ~50% whereas for the micrometer size the IQE is limited to values below 30%. We also observe that the boost of internal quantum efficiency for the smaller pillars corresponds to a large increase of the value of the spontaneous emission to around 8×10^9 s^{-1}. This large increase is a direct result of the reduction of the mode volume of the cavity resulting in an enhanced emission proportional to $1/V$. Despite having higher surface recombination for the smaller pillars, the reduction of the size is beneficial since allow us to achieve mode confinement and a small mode volume which has an impact in the radiative emission and corresponding increase of the IQE.

Figure 24 also shows inset the calculated IQE for the case where we are able to suppress the non-radiative part, that is, when the surface recombination velocity is much lower in the situation of passivated samples (in this case a value of 10^3 cm/s [34]). The results show extremely high efficiencies close to 99% for the pillars around 350 nm width. This clearly demonstrates that techniques that are able to passivate the walls of the pillars will be very beneficial to increase substantially the efficiency of nanoLEDs using pillar configurations.

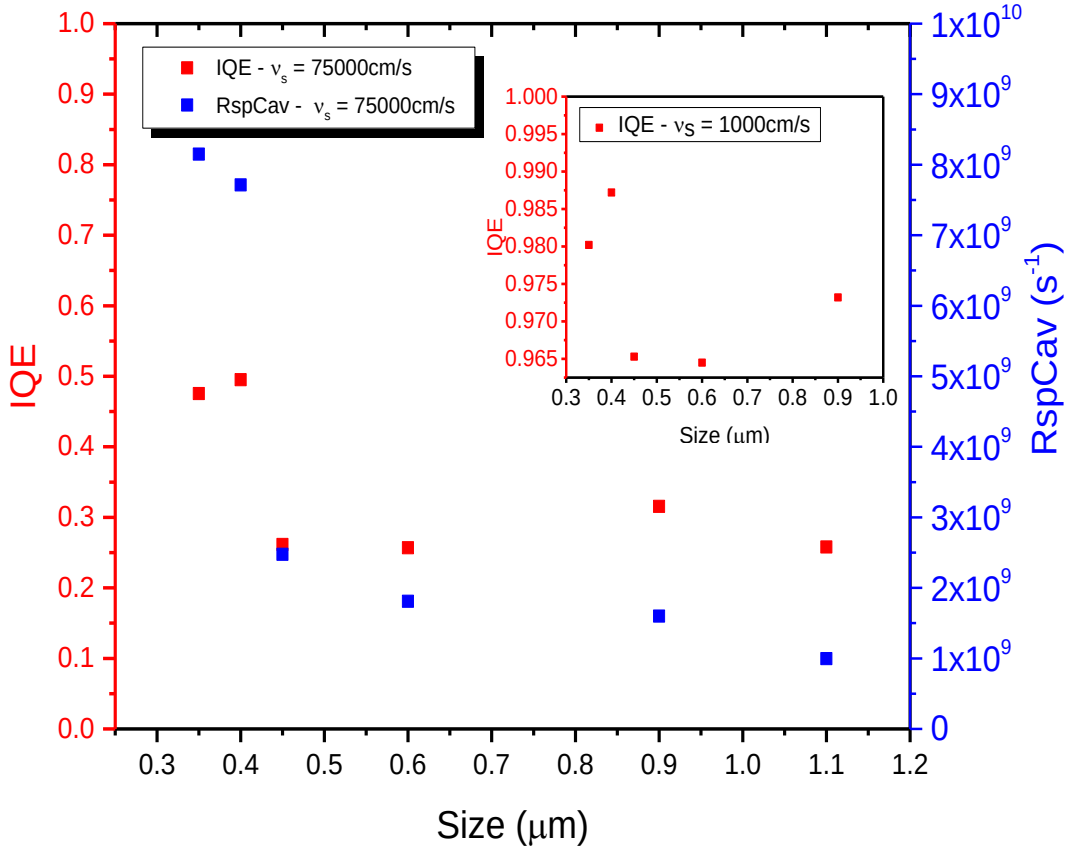

Figure 24 - Internal quantum efficiency for different sizes for the surface recombination velocity calculated in red and the respective spontaneous radiative result inside a cavity in blue. The inset shows the IQE for the same sizes using a lower surface recombination (the best results for GaAs in literature [34]).

In summary, using the values of surface recombination velocity extracted from the experimental data, the expected internal quantum efficiency (IQE) values of metallo-dielectric nanocavities were calculated and the potential of these structures for the design of efficient nanoLED sources was discussed. Further analysis includes to estimate the IQE as a function of the carrier density and include Auger recombination for the situation where the nanoLEDs are operating at high injection conditions. Also, the role of the non-homogenous mode profile in the active region of the metallo-dielectric nanocavities was not taken in consideration which may have an impact on the calculation of the spontaneous emission in the cavity.

4. Conclusion and Future Perspectives

In this thesis, we have investigated, both theoretically and experimentally, the optical properties of a metallic-cavity III-V AlGaAs/GaAs/AlGaAs semiconductor nanopillars for a broad range of sizes to estimate the internal quantum efficiency of these structures and analyze their potential efficient nanoLED sources. A 3-dimensional finite-difference time domain (3D-FDTD) was used to simulate the optical field distribution of metallo-dielectric nanopillar structures. The studies included the analysis of the optical field distribution, the Q-factor, resonance frequency, Purcell effect and mode volume. The simulations show that by designing the thickness of the cladding metal-dielectric layers the pillars of size ~350 nm show a typical mode volume ~0.01 μm^3 and Q-factors around 200 at a resonant wavelength close to 900 nm. These results show the benefits of adding a cavity in terms of Q-factor and light confinement when the size of the structures is well below one micrometer where light emitted in the cavity can be efficiently funneled to a single mode emission.

In the experimental results, methods of micro-photoluminescence and time-resolved photoluminescence were used to study the optical properties of AlGaAs/GaAs/AlGaAs semiconductor nanopillars. From the experimental results the corresponding lifetimes and peak intensity were analyzed. The lifetimes extracted from the measured time-resolved PL curves were used to obtain the surface recombination velocity value for each measured pillar. The surface recombination (non-radiative) results, showed values around 75000 cm/s of surface velocity for the largest pillars of 8 μm. Using the values of surface recombination velocity extracted from the experimental data, the expected internal quantum efficiency (IQE) values of metallo-dielectric nanocavities were analyzed.

As studied in [23] by placing an emitter in a small cavity, the photonic density of states can be enhanced by a factor $\propto Q/V$ as compared to the emission in the free space (or bulk), the famous "Purcell factor", while in our case for a broad emitter in a narrow cavity the photonic density of states is enhanced by a factor of $\propto 1/V$ [24]. The results show that taking advantage of the substantial reduction of the mode volume for the smaller pillars, efficiencies reaching values close to 50% can be achieved despite the fact the nanopillars suffer from higher surface recombination rates than the micropillars due to the large to surface to volume ratio. The importance of reducing the non-radiative effects using passivation methods was also analyzed showing that the efficiency of metallo-dielectric nanopillars can reach almost unity efficiency, with values up to 99%.

Despite the promising future of nanoLEDs there is still some challenges to take into account which include the nanofabrication of nanoLEDs with electrical carrier injection and methods of outcoupling of the light from the nanopillars. With this in mind, future studies include current injection efficiency and external quantum efficiency (EQE). In this thesis the injection used was based on optical pumping. The next step would be to inject electrical carriers and study the electroluminescence efficiency of this structure. Regarding the EQE, a future work includes the study of light outcoupling methods. For instance, one could test nano waveguides connected to the nanopillar.

The results of this master thesis show the potential of the nanoLEDs as an upcoming new alternative for photonic technologies in the development of novel optical sources for optical interconnects, biophotonics, bioimaging and neuromorphic computing applications.

5. References

[1] G. E. Moore, “Cramming more components onto integrated circuits, Reprinted from Electronics, volume 38, number 8, April 19, 1965, pp.114 ff.,” *IEEE Solid-State Circuits Soc. Newsl.*, vol. 11, no. 3, pp. 33–35, Sep. 2006.

[2] R. Kumar, P. Ranjan, and D. Das, “Moore’s Law,” pp. 508–514, 2016.

[3] N. Z. Haron and S. Hamdioui, “Why is CMOS scaling coming to an END?,” in *2008 3rd International Design and Test Workshop*, 2008, pp. 98–103.

[4] S. Fortuna, “Integrated Nanoscale Antenna-LED for On-Chip Optical Communication,” 2017.

[5] D. A. B. Miller, “Attojoule Optoelectronics for Low-Energy Information Processing and Communications,” *J. Light. Technol.*, vol. 35, no. 3, pp. 346–396, 2017.

[6] F. Pagliano *et al.*, “Waveguide-coupled nanopillar metal-cavity light-emitting diodes on silicon,” *Nat. Commun.*, vol. 8, pp. 1–8, 2017.

[7] J. Leuthold *et al.*, “Plasmonic Communications: Light on a Wire,” *Opt. Photon. News*, vol. 24, no. 5, pp. 28–35, May 2013.

[8] R. Michalzik, *VCSELs : fundamentals, technology and applications of vertical-cavity surface-emitting lasers*. Springer, 2013.

[9] R. M. Ma and R. F. Oulton, “Applications of nanolasers,” *Nat. Nanotechnol.*, vol. 14, no. 1, pp. 12–22, 2019.

[10] B. Ellis *et al.*, “Ultralow-threshold electrically pumped quantum-dot photonic-crystal nanocavity laser,” *Nat. Photonics*, vol. 5, no. 5, pp. 297–300, 2011.

[11] M. T. Hill *et al.*, “Lasing in metallic-coated nanocavities,” *Nat. Photonics*, vol. 1, no. 10, pp. 589–594, 2007.

[12] R. F. Oulton *et al.*, “Plasmon lasers at deep subwavelength scale,” *Nature*, vol. 461, no. 7264, pp. 629–632, 2009.

[13] D. Calzadilla, *Metal nanocavity light sources integrated with passive waveguide components*, no. april. 2016.

[14] K. C. Y. Huang, M. Seo, T. Sarmiento, Y. Huo, J. S. Harris, and M. L. Brongersma, “Electrically driven subwavelength optical nanocircuits,” no. February, 2014.

[15] B. Romeira and A. Fiore, “Physical Limits of NanoLEDs and Nanolasers for Optical Communications,” *Proc. IEEE*, no. 1, pp. 1–14, 2019.

[16] E. K. Lau, A. Lakhani, R. S. Tucker, and M. C. Wu, “Enhanced modulation bandwidth of nanocavity light emitting devices,” *Opt. Express*, vol. 17, no. 10, p. 7790, May 2009.

[17] B. Romeira *et al.*, “Ultralow Surface Recombination Velocity in Passivated InGaAs/InP Nanopillars,” 2017.

[18] H. Küpers *et al.*, “Impact of Outer Shell Structure and Localization Effects on Charge Carrier Dynamics in GaAs /(In , Ga) As Nanowire Core – Shell Quantum Wells,” vol. 1800527, pp. 1–5, 2019.

[19] “CHIPAI.” [Online]. Available: https://www.chipai.eu/. [Accessed: 13-Sep-2019].

[20] U. Strauss, W. W. Rühle, and K. Köhler, “Auger recombination in intrinsic GaAs,” *Appl. Phys. Lett.*, vol. 62, no. 1, pp. 55–57, 1993.

[21] “Inhibited and enhanced spontaneous emission from optically thin AlGaAs/GaAs Double

Heterostructures," *Phys. Rev. Lett.*, vol. 61, no. 22, pp. 2546–2549, 1988.

[22] Y. Wan, "Radiative and Nonradiative Recombination," vol. 0, no. 6, pp. 1–18, 2003.

[23] E. M. Purcell, "Spontaneous Emission Probabilities at Radio Frequencies," 1995, pp. 839–839.

[24] B. Romeira and A. Fiore, "Purcell Effect in the Stimulated and Spontaneous Emission Rates of Nanoscale Semiconductor Lasers," *IEEE J. Quantum Electron.*, vol. 54, no. 2, pp. 1–12, 2018.

[25] H. Altug, D. Englund, and J. Vučković, "Ultrafast photonic crystal nanocavity laser," *Nat. Phys.*, vol. 2, p. 484, Jul. 2006.

[26] G. Shambat *et al.*, "Ultrafast direct modulation of a single-mode photonic crystal nanocavity light-emitting diode," *Nat. Commun.*, vol. 2, no. 1, p. 539, 2011.

[27] "High-Performance Photonic Simulation Software - Lumerical." [Online]. Available: https://www.lumerical.com/. [Accessed: 22-Sep-2019].

[28] M. Wahl, "PicoQuant- Time-Correlated Single Photon Counting The Principle of Time-Correlated," pp. 1–14, 2017.

[29] J. Enderlein and R. Erdmann, "Fast fitting of multi-exponential decay curves," *Opt. Commun.*, vol. 134, no. 1–6, pp. 371–378, Jan. 1997.

[30] R. K. Ahrenkiel and M. S. Lundstrom, *Minority Carriers in III-V Semiconductors: Physics and Applications*, no. vol. 39. Academic Press, 1993.

[31] R. Dändliker, "The concept of mode in optics and photonics," vol. 3831, pp. 193–198, 2000.

[32] G. Grzela, *Directional light emission and absorption by semiconductor naowires*. 2013.

[33] B. Romeira, J. Borme, H. Fonseca, J. Gaspar, and J. B. Nieder, "Strong Enhancement of Light Extraction Efficiency in Sub-wavelength AlGaAs/GaAs Vertical-emitting Nanopillars," in *2019 Conference on Lasers and Electro-Optics Europe and European Quantum Electronics Conference*, 2019, p. ck_3_6.

[34] E. Yablonovitch, C. J. Sandroff, R. Bhat, and T. Gmitter, "Nearly ideal electronic properties of sulfide coated GaAs surfaces," *Appl. Phys. Lett.*, vol. 51, no. 6, pp. 439–441, 1987.

6. Appendix

Time resolved photoluminescence from nanopillars

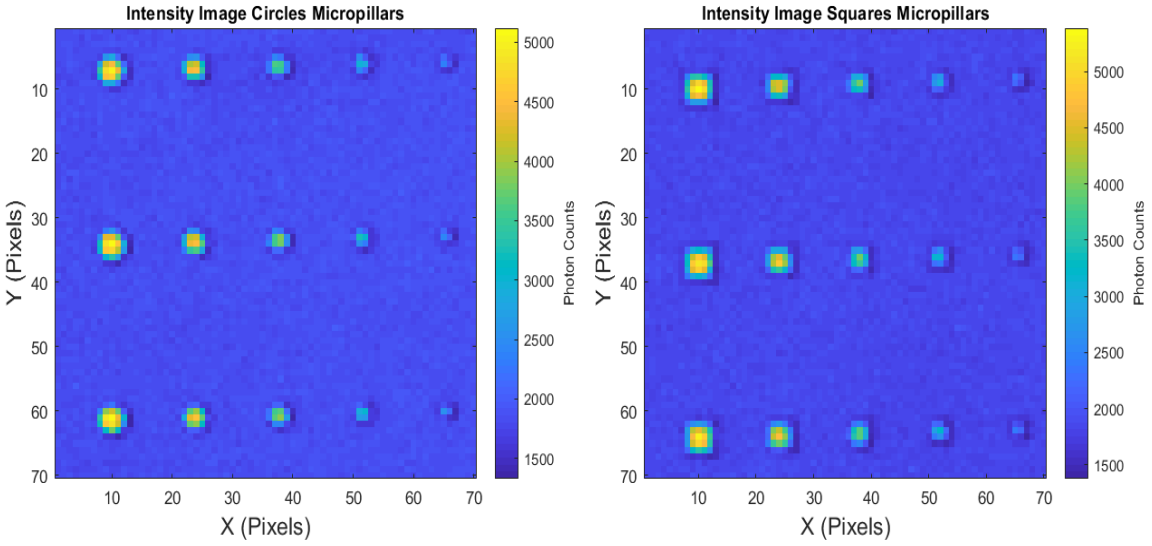

a) b)

Figure 25 - Intensity images obtained using the FLIM setup for a) circular micropillars and b) square micropillars ranging from 8 µm to 4 µm under 561 nm pulsed excitation.